Low-frequency modulation of flutter oscillations: a Floquet analysis based on the Time Spectral Method

Johann Moulin[1] † and Olivier Marquet[1]

[1]ONERA-DAAA, 8 rue des Vertugadins, 92190 Meudon, France

(Received xx; revised xx; accepted xx)

The flutter oscillations of a thin plate mounted on a system of bending/torsional springs and immersed in a laminar incompressible flow are investigated numerically for the low Reynolds number $Re = 500$ and the large solid-to-fluid mass ratio $\tilde{m} = 1000$. Time-marching simulations of the fluid-solid interaction first show that, when increasing the reduced velocity above the critical value U_c^*, periodic oscillations of the plate are first observed, resulting from a *primary* flutter instability of the steeady solution. For these low-frequency oscillations ($\omega_0 \sim 0.15$), the flow is quasi-steady and remains attached to the plate during (almost) the whole period. For slightly larger reduced velocity, a very-low-frequency modulation of the pitching angle is then observed, associated to stronger flow separation occurring when the pitching angle oscillates between larger values. Drawing a Poincaré map clearly indicates that the quasi-periodic solution is a torus attractor. To explain the emergence of the quasi-periodic solutions, a secondary instability analysis is then achieved, based on a Floquet analysis that fully relies on the Time Spectral Method, not only to compute the unstable periodic limit cycle oscillations, but also to determine the leading Floquet modes. We thus show that an asynchronous Floquet mode gets unstable for values of the reduced velocity where quasi-periodic solutions are observed. Their very-low frequency ω is well predicted by the Floquet analysis, especially slightly above the secondary critical velocity. An analysis of the pitching and heaving component of the complex Floquet mode shows that they are almost in phase for their real part, but out-of-phase for the imaginary part. A spectral analysis of these Floquet components further reveals that the pitching angle predominantly oscillates at a slightly higher frequency $\omega_0 + \omega$) than the heaving displacement which oscillates (predominantly) at $\omega_0 - \omega$, in agreement with results of nonlinear simulations. This explains that the phase difference between the pitching and heaving signal continuously drifts during the very-slow oscillation. The recontruction of this oscillating components allows to better understand the physical origin of the very-low-frequency modulation. When the pitching (resp. heaving) motion precedes the heaving (resp. pitching) motion, energy is extracted from (resp. transmitted to) the flow and the plate exhibits a flutter (resp. anti-flutter) motion.

1. Introduction

The flutter linear instability that occurs on a heaving and pitching spring-mounted typical section (Dowell *et al.* 1989, §3.3.5) gives a rise to a Hopf bifurcation, as the consequence of the destabilization of a pair of complex conjugate fluid-structure eigenmodes of the steady configuration where the section is horizontal. For reduced velocities above the critical threshold for flutter, this pair of eigenmodes grows exponentially until the system's nonlinearity come into play and saturate their growth. Then, periodic regimes with well defined amplitude, referred to as *Limit Cycle Oscillations* (LCO), are observed. In the case of a supercritical flutter bifurcation, that we investigate here, the amplitude of the LCO is usually expected to grow smoothly as the reduced velocity increases. However, LCO solutions — just like steady solutions — can

† Email address for correspondence: johann.moulin@onera.fr

be unstable and transition, through secondary instabilities, to richer temporal behaviors, like quasi-periodic oscillations or even chaos (Nayfeh & Balachandran 1995).

Several researchers have reported the destabilization of flutter LCO on two degrees of freedom spring-mounted typical aeroelastic sections. The vast majority of these works investigated various types of nonlinearities in the structure, while keeping the fluid modeling linear (steady, quasi-steady or Theodorsen models). For example, in (Liu & Dowell 2004; Lee *et al.* 2005), a cubic stiffness nonlinearity in the pitch spring and coupled to Theodorsen's model for the fluid was investigated. In (Zhang & Chen 2017; Liu *et al.* 2018), the cubic stiffness was put in the degree of freedom governing an added external store while steady thin airfoil theory was used for the fluid. These authors showed that for high enough reduced velocities, the flutter LCO undergoes low-frequency amplitude modulations, which are attributed to the destabilization of a pair of complex conjugate Floquet modes (Liu *et al.* 2018). Using different types of structural nonlinearities, *e.g.* freeplay or hysteresis, a wide zoology of dynamics may be observed, as exposed in the comprehensive review by Lee *et al.* (1999). Regarding the effect of fluid nonlinearities, the literature is much scarcer and — to the authors' best knowledge — always based on empirical dynamic stall models. Using such a fluid model, Li & Fleeter (1997) showed that a structurally linear airfoil with nonzero static angle of attack transitions from stable static equilibrium, to flutter LCO, and finally to chaos, through a "quasi-periodic route to chaos". More recently, similar quasi-periodic oscillations were reported in (Jian & Jinwu 2009), for a structurally nonlinear high-aspect-ratio wing.

Mathematically, the asymptotic linear stability of a periodic orbit is carried on using Floquet stability analysis (Floquet 1883). This analysis typically consists in computing the so-called Floquet multipliers, that are complex numbers that quantify the growth/decay and frequency of infinitesimal perturbations that may develop on top of a previously established LCO. The most widely spread numerical approach is to obtain the Floquet multipliers as the eigenvalues of the *monodromy matrix* $\mathbf{\Phi}$, defined as the operator that propagates a perturbation $\mathbf{q}'(t)$ over one period T_0 of the LCO: $\mathbf{q}'(t+T_0) = \mathbf{\Phi}\mathbf{q}'(t)$. Building $\mathbf{\Phi}$ can be quite a cumbersome task, as it requires K (K being the number of degrees of freedom) time-integrations of the linearized governing equations, across one period T_0. More details on different variants of this approach can be found, for example, in (Peletan *et al.* 2013). When high-dimensional physical models — typically, the spatially discretized Navier–Stokes equations — are used, K becomes so large that building $\mathbf{\Phi}$ is not feasible. In that case, only a few dominant Floquet multipliers are computed, using Arnoldi type algorithms (Barkley & Henderson 1996; Elston *et al.* 2004; Deng & Caulfield 2016; Jallas *et al.* 2017; Shaabani-Ardali *et al.* 2019). In this case, the linearized governing equations must be time-marched only a number of time equal to the size of the Krylov subspace times the number of Arnoldi iterations, which is always much smaller than K. In these approaches, based on time-marching the linearized equations, another challenge is to first compute the base LCO solution of which Floquet stability is then computed. If the LCO is stable, this can be simply done by time-marching the nonlinear equations on a long enough interval of time. If the LCO is unstable however, stabilization techniques must be devised in order for the time-marching approach to settle on these naturally unstable LCO solutions. Several methods have been proposed to achieve such a task, but are often based on the prior knowledge of a property of the targeted LCO. For example, if the LCO is known to possess some spatial symmetry, the latter can be directly imposed in the time-marching algorithm (Elston *et al.* 2004; Deng & Caulfield 2016). When only a spatio-temporal symmetry property of the LCO is known, specific stabilization techniques are used to artificially damp the symmetry-breaking components from the time-marching solution (Jallas *et al.* 2017; Shaabani-Ardali *et al.* 2019). In parallel to these time-domain approaches, some researcher (Liu & Dowell 2004; Liu *et al.* 2018) have opted for frequency-domain approaches, often referred to as Harmonic Balance Methods (HBM). These methods impose the temporal periodicity of the researched solution by decomposing it as a (truncated) Fourier series. As a consequence,

no *a priori* knowledge on the LCO is required to compute it, which gives HBM a significant advantage over the aforementioned time-domain approaches. The reader is reported to **??** for extensive details on Harmonic Balance Methods. In addition to its ability to arbitrary compute LCO's regardless of their stability, HBM also offers the capacity to assess Floquet stability by computing the Floquet exponents as the eigenvalues of the linearized HBM equations (Deconinck & Nathan Kutz 2006; Lazarus & Thomas 2010; Krack & Gross 2019). As a consequence, and despite some known shortcomings mostly related to sorting the Floquet exponents (Lazarus & Thomas 2010), Harmonic Balance Methods appear as an appealing alternative for LCO stability analysis.

In this work, we study the stability of flutter LCO solutions that develop on a two degrees of freedom spring-mounted plate, immersed in a viscous incompressible flow. Whereas the solid model is purely linear, we are interested in the effect of the fluid nonlinearities, contained in the Navier–Stokes equations. To that purpose, we use a particular type of HBM, referred to as the Time Spectral Method (TSM) (Gopinath & Jameson 2005) to efficiently compute flutter LCO's. The TSM equations are solved thanks to the Newton–Krylov solver previously developed in **??**. Then, we show how the Floquet stability of those LCO's can be assessed through an eigenvalue analysis of the Jacobian of the TSM equations. An advantage of this approach is that it naturally fits in the TSM framework and heavily relies on routines already developed for the Newton–Krylov TSM solver.

The rest of the chapter organizes as follows. Section 2 starts by a brief summary of the equations governing the motion of the spring-mounted plate. Then, after recalling some elements of Floquet theory (section 2.2), we introduce in section 2.3 a TSM-based approach for first computing periodic flutter solutions and then assessing their Floquet stability. Section 3 gathers the presentation and analysis of the numerical results. We start by reporting in section 3.1, using time-marching computations, the emergence of low-frequency modulations on top of small amplitude flutter LCO's, for high-enough reduced velocities. Then, in section 3.2, these modulations are explained by a linear instability of the flutter LCO, due to the destabilization of a pair of complex conjugate Floquet modes. In section 3.3, we reconstruct the physical perturbation associated to the pair of unstable modes, allowing us to shed some light on the physical mechanism governing the appearance of the low-frequency modulation in the fully nonlinear time-marching solutions (section 3.4).

2. Governing equations and TSM-based numerical approach for Floquet stability analysis

2.1. *Governing equations*

We investigate the non-linear dynamics of a rigid plate mounted on heaving and pitching springs with respective stiffness K_h and K_θ and immersed in a two-dimensional incompressible viscous open flow with far-field velocity U_∞. As discussed in section **??**, eight non-dimensional parameters defined in **??**, govern that fluid-structure interaction problem, namely, the heaving-to-pitching frequency ratio Ω, the structural damping ratios ζ_h, ζ_p, the radius of gyration r_θ, the position of the elastic axis x_θ (zero here), the solid-to-fluid mass ratio $\tilde{m}$, the Reynolds number Re and the reduced velocity U^* In this chapter, only the reduced velocity is varied while all other parameters are kept fixed to values specified latter. The reduced velocity is defined as the ratio of the far-field fluid velocity to a velocity typical of the natural pitching mode, $U^* = U_\infty/(c\sqrt{K_\theta/I_{\text{ea}}})$, where c is the plate's chord and I_{ea} is its moment of inertia with respect to the elastic axis.

The dynamics of the spring-mounted plate is governed by two (damped) linear oscillator

equations **??**, that are recalled here:

$$\frac{\partial^2 h}{\partial t^2} + 2\zeta_h \left(\frac{\Omega}{U^*}\right) \frac{\partial h}{\partial t} + \left(\frac{\Omega}{U^*}\right)^2 h = \frac{1}{\tilde{m}} C_L \tag{2.1a}$$

$$\frac{\partial^2 \theta}{\partial t^2} + 2\zeta_p \left(\frac{1}{U^*}\right) \frac{\partial \theta}{\partial t} + \left(\frac{1}{U^*}\right)^2 \theta = \frac{1}{\tilde{m} {r_\theta}^2} C_M \tag{2.1b}$$

with C_L the lift coefficient and C_M the moment coefficients about the elastic axis (which is the mid-chord here). The flow is modeled with the two-dimensional incompressible Navier–Stokes equations, for which an Arbitrary Lagrangian-Eulerian (ALE) framework (written in a reference domain) is used to handle fluid domain motion (Pfister *et al.* 2019). The equations have been previously stated in **??** (see **??**) to which the interested reader is reported for more details.

In the following, the coupled system constituted by the solid and fluid equations is written formally as a first-order in time evolution operator:

$$\mathscr{M}(\mathbf{q}) \frac{\partial \mathbf{q}}{\partial t} + \mathscr{R}(\mathbf{q}) = 0 \tag{2.2}$$

where the variable $\mathbf{q} = (h, \theta, u_h, u_\theta, \mathbf{u}, p, \boldsymbol{\lambda})^{\mathrm{T}}$ gathers all variables necessary to describe the fluid-solid interaction. The first four scalar variables allow describing the dynamics of the rigid plate. They are the heaving h and pitching θ displacements, as well as the corresponding velocities u_h and u_θ. The incompressible flow is described with the velocity $\mathbf{u}$ and pressure p fields. Finally, the variable $\boldsymbol{\lambda}$, defined at the fluid-solid interface, represents the local stress exerted by the fluid onto the solid. System (2.2) is composed of seven equations: the first four correspond to the solid modeleq. (2.1), written as a first-order problem in time. The fifth and sixth equations are the Navier–Stokes momentum and mass conservation equations. The last equation corresponds to the equality of fluid and solid velocities at the fluid-solid interface. Note that the mass matrix $\mathscr{M}(\mathbf{q})$ depends here on the unknown solution $\mathbf{q}$. This is due to the particular reference configuration ALE framework used to formulate the Navier–Stokes equations, where the Jacobian of the mesh deformation field appears in front of the time derivative (see **??**).

2.2. *Linear stability analysis of Limit Cycle Oscillations*

Limit Cycle Oscillations (LCO) are periodic solutions $\mathbf{q}_0(t)$ of (2.2) that can loose stability *via* linear instabilities. In this work, the linear stability of LCO's is assessed through a Floquet stability analysis which consists in evaluating the asymptotic stability of perturbations $\mathbf{q}'$ that develop around the LCO. To that aim, the solution is decomposed as

$$\mathbf{q}(t) = \mathbf{q}_0(t) + \epsilon\, \mathbf{q}'(t) \qquad\qquad \epsilon \ll 1 \tag{2.3}$$

the sum of the periodic solution and an infinitesimal perturbation $\mathbf{q}'(t)$. By injecting this *ansatz* solution in eq. (2.2), we obtain at order ϵ^0 the equation governing the LCO, i.e.

$$\mathscr{M}(\mathbf{q}_0) \frac{\partial \mathbf{q}_0}{\partial t} + \mathscr{R}(\mathbf{q}_0) = 0 \qquad \text{with} \qquad \mathbf{q}_0(t + T_0) = \mathbf{q}_0(t) \tag{2.4}$$

and at order ϵ^1 the equation governing the perturbation, i.e.

$$\mathscr{M}(\mathbf{q}_0(t)) \frac{\partial \mathbf{q}'}{\partial t} + \mathscr{J}(\mathbf{q}_0(t))\, \mathbf{q}' = 0 \tag{2.5}$$

where the Jacobian operator of the coupled problem, linearized around $\mathbf{q}_0$, is defined as

$$\mathscr{J}(\mathbf{q}_0(t)) = \partial\mathscr{R}/\partial\mathbf{q}|_{\mathbf{q}_0(t)} + \partial\mathscr{M}/\partial\mathbf{q}|_{\mathbf{q}_0(t)}\ \partial\mathbf{q}_0/\partial t$$

In the present fluid-structure formulation, since the mass matrix depends on the state variable, the derivative of $\mathscr{M}(\mathbf{q})$ to that state vector appears in the definition of $\mathscr{J}(\mathbf{q})$. Obviously, for

physical systems with formalism less intricate than the present one, $\mathscr{M}$ is generally a constant mass matrix, and we simply retrieve $\mathscr{J}(\mathbf{q}_0(t)) = \partial\mathscr{R}/\partial\mathbf{q}|_{\mathbf{q}_0(t)}$.
Following Floquet's theory (Floquet 1883), the solutions to a linear system with periodic coefficients, like eq. (2.5), can be found as a superposition of *Floquet form* signals:

$$\mathbf{q}'(t) = \mathbf{q}^\circ(t)e^{\sigma t} + \text{c.c.} \tag{2.6}$$

where $\mathbf{q}^\circ(t)$ is a T_0-periodic function, called *Floquet mode*, and $\sigma = \lambda + \mathbf{i}\omega \in \mathbb{C}$ is the *Floquet exponent*. Inserting the Floquet form in eq. (2.5) we find that $(\sigma, \mathbf{q}^\circ(t))$ are (generalized) eigenpairs of a spatio-temporal linear operator:

$$\sigma\mathscr{M}(\mathbf{q}_0(t))\,\mathbf{q}^\circ + \left(\mathscr{M}(\mathbf{q}_0(t))\,\frac{\partial}{\partial t} + \mathscr{J}(\mathbf{q}_0(t))\right)\mathbf{q}^\circ = 0 \tag{2.7}$$

By solving eq. (2.7), the linear stability of the base LCO $\mathbf{q}_0(t)$ is thus determined from the growth rate of the Floquet exponents λ. If all $\lambda < 0$, then any perturbation is asymptotically damped and the LCO is linearly asymptotically stable. On the contrary, if at least one exponent verifies $\lambda > 0$, the corresponding perturbation grows exponentially and the LCO is linearly unstable. In the next paragraph, we focus on the numerical solution of the base LCO problem eq. (2.4) and the Floquet eigenproblem eq. (2.7) using a type of space-time discretization, called Time Spectral Method, well-suited to periodic problems.

2.3. *A Time Spectral Method-based approach for Floquet stability analysis*

The Time Spectral Method (Gopinath & Jameson 2005) is used for the computation of the LCO (2.4) and of the Floquet exponents/modes (2.7). It consists in discretizing time on a periodic grid $t_n = T_0 n/(2N+1)$, $n = 0, \ldots, 2N$ of $2N+1$ instants, where $T_0 = 2\pi/\omega_0$ is the (*a priori* unknown) period of the solution and N is the number of harmonics captured. The time derivative of any periodic field is approximated at the grid points using a spectral approximation:

$$\left.\frac{\partial\mathbf{q}}{\partial t}\right|(t_n) \simeq \omega_0 \sum_{k=0}^{2N} d_k\,\mathbf{q}(t_{n+k}) \tag{2.8}$$

where the coefficients d_k are given by

$$d_k = \begin{cases} \dfrac{1}{2}(-1)^{k+1}\csc\left(\dfrac{\pi k}{2N+1}\right) & \text{if } k \neq 0 \\ 0 & \text{if } k = 0 \end{cases}$$

LCO computation based on TSM Using the spectral time-derivative approximation eq. (2.8), the time-dependent equations (2.4) governing the LCO can be recast into a system of $2N+1$ coupled time-independent equations that writes:

$$\omega_0\,\mathbf{D}\,\mathbf{Q}_0 + \mathbf{R}(\mathbf{Q}_0) = 0 \tag{2.9}$$

where the solution and residual vector are

$$\mathbf{Q}_0 = \begin{pmatrix} \mathbf{q}_0(t_0) \\ \vdots \\ \mathbf{q}_0(t_{2N}) \end{pmatrix} \text{ and } \mathbf{R}(\mathbf{Q}_0) = \begin{pmatrix} \mathscr{R}(\mathbf{q}_0(t_0)) \\ \vdots \\ \mathscr{R}(\mathbf{q}_0(t_{2N})) \end{pmatrix} \tag{2.10}$$

and the time-spectral derivative matrix is defined as

$$\mathbf{D} = \begin{pmatrix} 0 & d_1\,\mathscr{M}(\mathbf{q}_0(t_0)) & \dots & d_{2N}\,\mathscr{M}(\mathbf{q}_0(t_0)) \\ d_{2N}\,\mathscr{M}(\mathbf{q}_0(t_1)) & 0 & \ddots & \\ & \ddots & \ddots & d_1\,\mathscr{M}(\mathbf{q}_0(t_{2N-1})) \\ d_1\,\mathscr{M}(\mathbf{q}_0(t_{2N})) & & d_{2N}\,\mathscr{M}(\mathbf{q}_0(t_{2N})) & 0 \end{pmatrix} \tag{2.11}$$

Since the frequency ω_0 is unknown, an additional equation is necessary to close the system. In practice, this equation is an arbitrary condition that fixes the phase of the LCO. In this work, we chose impose that the pitching velocity is zero, $u_\theta = 0$, at instant $t = 0$. Finally, we mention that in our TSM solver, the reduced velocity U^* is not directly imposed as a parameter. Instead, it is a second additional unknown of the problem. As for the frequency, a new scalar equation is provided to close the system, and consists in imposing the amplitude $\theta_{\max}$ of the pitching motion.

The TSM problem eq. (2.9), augmented with the additional phase and amplitude constraints introduced above is a nonlinear system of equation with a large number of degrees of freedom, $(2N+1)\times K + 2$ with K the number of degrees of freedom corresponding to the finite element spatial discretization of $\mathbf{q}$. This problem is solved using a Newton–Krylov approach that combines classical Newton iterations with a Krylov subspace linear solver (Saad 1993) to tackle the challenging high-dimensional linear problems arising at each Newton iteration. An adequate preconditioner for the Krylov method, proposed in **??**, is built using the so-called block-circulant preconditioner for the TSM equations and a Schur complement approach for the two additional scalar (phase and amplitude) constraints. The interested reader will find extensive details regarding the formulation, implementation, validation and numerical performance of the above described TSM solver in **??**.

Floquet mode/exponent computation based on TSM The eigenproblem eq. (2.7) is discretized in time and space using again the Time Spectral and Finite Element methods, respectively. This yields the following fully discrete problem of dimension $(2N+1)\times K$:

$$\sigma \mathbf{M}\,\mathbf{Q}^\circ + (\omega_0 \mathbf{D} + \mathbf{J})\,\mathbf{Q}^\circ = 0 \tag{2.12}$$

where $\sigma = \lambda + \mathbf{i}\omega$ is the complex Floquet exponent associated to the Floquet mode $\mathbf{Q}^\circ$, defined as

$$\mathbf{Q}^\circ = \begin{pmatrix} \mathbf{q}^\circ(t_0) \\ \vdots \\ \mathbf{q}^\circ(t_{2N}) \end{pmatrix}$$

The block-diagonal mass $\mathbf{M}$ and Jacobian $\mathbf{J}$ matrices write

$$\mathbf{M} = \begin{pmatrix} \mathscr{M}(\mathbf{q}_0(t_0)) & 0 & \dots & 0 \\ 0 & \mathscr{M}(\mathbf{q}_0(t_1)) & \ddots & \vdots \\ \vdots & \ddots & \ddots & 0 \\ 0 & \dots & 0 & \mathscr{M}(\mathbf{q}_0(t_{2N})) \end{pmatrix} \quad \text{and}$$

$$\mathbf{J} = \begin{pmatrix} \mathscr{J}(\mathbf{q}_0(t_0)) & 0 & \dots & 0 \\ 0 & \mathscr{J}(\mathbf{q}_0(t_1)) & \ddots & \vdots \\ \vdots & \ddots & \ddots & 0 \\ 0 & \dots & 0 & \mathscr{J}(\mathbf{q}_0(t_{2N})) \end{pmatrix}$$

At this stage, it must be mentioned that the proposed approach is found to be very similar

Krylov–Schur it.	Linear solver calls	total GMRES it.	Wall-clock time
6	714	27,540	1h06min

Table 1: Cost of a Krylov–Schur run for the following numerical parameters: $s = 1 + 0\mathbf{i}$, $n_{ev} = 40$, $n_{cv} = 200$, $N = 5$, $\text{tol}_{\text{GMRES}} = \text{tol}_{\text{KS}} = 10^{-6}$. The corresponding spectrum is shown in fig. 1(a).

to the Floquet–Fourier–Hill method, originally devised as an analytical tool by Hill (1886), and more recently re-popularized as a numerical method (Deconinck & Nathan Kutz 2006; Lazarus & Thomas 2010). The major difference resides in the fact that in the Floquet–Fourier–Hill method, a frequency-domain Harmonic Balance discretization of eq. (2.7) is used, instead of a time-domain here.

Numerical solution of the Floquet eigenproblem The size of the matrices involved in eq. (2.12) is $(2N+1)K \times (2N+1)K$, which quickly grows with both the spatial discretization (N) and the temporal discretization (K). As a consequence — and contrary to previous works (Deconinck & Nathan Kutz 2006; Lazarus & Thomas 2010) who focused on low-dimensional systems, $K \simeq O(1)$ —, the spectrum of eq. (2.12) cannot be obtained at reasonable cost with classical dense algebra algorithms, even for low N. Instead, we perform Krylov–Schur iterations on the *shifted-and-inverted* eigenproblem :

$$\widetilde{\sigma}\mathbf{Q}^{\circ} + \mathbf{T}\mathbf{Q}^{\circ} = 0$$
$$\text{with} \quad \widetilde{\sigma} = (\sigma - s)^{-1} \qquad \text{and} \qquad \mathbf{T} = \left[s\mathbf{M} + (\omega_0\mathbf{D} + \mathbf{J})\right]^{-1}\mathbf{M}$$

in order to converge a few eigenvalues of interest, near the user-defined shift $s \in \mathbb{C}$. By moving s along the imaginary axis ($\lambda \simeq 0$), one can monitor the destabilization of Floquet modes. As only matrix-vector products with $\mathbf{T}$ are needed in the Krylov–Schur iterations, $\mathbf{T}$ is never assembled. Only its action $\mathbf{x} = \mathbf{T}\mathbf{z}$ on a given vector $\mathbf{z}$ is computed through one matrix-vector product $\mathbf{y} = \mathbf{M}\mathbf{z}$ and one solve of the linear system $\left[s\mathbf{M} + (\omega_0\mathbf{D} + \mathbf{J})\right]\mathbf{x} = \mathbf{y}$. Finally, noticing that the latter system is very similar to a Newton step of the nonlinear TSM solver, we simply re-use the block-circulant preconditioned GMRES solver already used in the nonlinear solver (see **??**). The typical cost of a Krylov–Schur run is presented in table 1 where we compute the 40 Floquet multipliers closest to the (real-valued for this case) shift $s = 1$, using $N = 5$ harmonics (*i.e* 11 temporal grid points). The obtained spectrum is the one presented in fig. 1(a). With a Krylov space of size 200, we need 6 Krylov–Schur interations to converge all 40 eigenvalues to 10^{-6}. This corresponds to 714 linear solves (GMRES calls), for a total amount of 27,540 GMRES iterations (*i.e.* as much applications of the circulant preconditioner and matrix-vector product with $[s\mathbf{M} + (\omega_0\mathbf{D} + \mathbf{J})]$). This corresponds to about 40 GMRES iterations per linear solve. Using the time-parallel implementation detailed in **??**, the total wall-clock time is about an hour.

Overall, it appears that most of the matrices and routines involved in the building and subsequent solution of eq. (2.12) are bricks of the Newton-Krylov TSM solver used for computing LCO solutions. In particular, the matrix $\omega_0\mathbf{D} + \mathbf{J}$ is simply the Jacobian of the TSM system, eq. (2.9). As a consequence, the Floquet eigenproblem can be assembled and solved by moslty re-using the computational routines of the nonlinear solver. From a practical point of view, we point out however that all computational routines must be adapted to handle complex algebra if one is to use a shift with nonzero imaginary part.

Periodicity of the Floquet exponents and choice of the relevant modes In this paragraph we point out the periodicity property of the Floquet exponents and explain how it affects the choice of the physically relevant eigenpairs amongst all eigenpairs $(\sigma, \mathbf{q}^\circ(t))$ of eq. (2.12).

In fig. 1(a), we show a typical spectrum of the leading Floquet exponents obtained from the numerical solution of eq. (2.12). The spectrum presents a repeating pattern — except at the upper and lower extremities, on which we will come back below — along the imaginary axis, with period ω_0. The observed periodicity of the Floquet exponents originates from the fact that the Floquet form of the linear perturbation $\mathbf{q}'(t)$, introduced in eq. (2.6), in fact admits an infinity of equivalent representations, indexed by the integer $p \in \mathbb{Z}$:

$$\mathbf{q}'(t) = \mathbf{q}^{\circ,p}(t) e^{(\sigma + \mathbf{i} p\, \omega_0) t} + \text{c.c.} \qquad \text{with} \qquad \mathbf{q}^{\circ,p}(t) = \sum_{n=-\infty}^{\infty} \widehat{\mathbf{q}^\circ}_n e^{\mathbf{i}(n-p)\omega_0 t} \tag{2.13}$$

where the $\widehat{\mathbf{q}^\circ}_n$ are the Fourier coefficients of the ω_0-periodic Floquet mode:

$$\mathbf{q}^\circ(t) = \sum_{n=-\infty}^{\infty} \widehat{\mathbf{q}^\circ}_n e^{\mathbf{i} n \omega_0 t}$$

Varying the index p simply "displaces" multiples of the base LCO frequency ω_0 from the Floquet mode to the Floquet exponent and *vice-versa*. However, the real physical perturbation $\mathbf{q}'(t)$ associated to each couple $(\sigma + \mathbf{i} p\omega_0, \mathbf{q}^{\circ,p}(t))$ is left unchanged by changing p, as shown by eq. (2.13). As a direct consequence, it is easily verified that if $(\sigma, \mathbf{q}^\circ(t))$ is an eigenpair of eq. (2.7), then all the $(\sigma + \mathbf{i} p\omega_0, \mathbf{q}^{\circ,p}(t))$, $p \in \mathbb{Z}$ are also eigenpairs. Thus, the spectrum of Floquet exponents is $\mathbf{i}\omega_0$-periodic, as observed in fig. 1(a).

In theory, this periodicity implies that only the eigenvalues in a section of the complex plane of extension ω_0 along the imaginary axis are representative of the whole spectrum. In practice however, truncation effects due to finite N (here $N = 5$) break that periodicity, as observed in the upper and lower extremities of the spectrum in fig. 1(a). The physically relevant eigenvalues (*i.e.* the ones that respect the periodicity) must then be carefully separated from the non-relevant ones (*i.e.* the ones that break the periodicity). In this work, the distinction is made by looking at the Fourier spectrum of the corresponding Floquet mode. As an example, we show in fig. 1(b) the Fourier spectrum of the dominant Floquet exponent (marked by a gray disk in (a)). If the harmonics of the mode well decrease to zero on the extremities of the computational spectrum $[-N\omega_0, N\omega_0]$ (*e.g.* the central Fourier spectrum in (b)), then the mode is well converged (in time), and thus physically relevant. On the contrary, if the harmonics are large at one of the extremities of the Fourier spectrum (see the upper or lower spectra in (b)), then the mode is ill-converged and thus discarded for physical analysis. Once all ill-converged exponents have been excluded, it is usually more convenient to represent LCO stability using the Floquet multipliers $\mu = e^{\sigma T_0}$ represented in fig. 1(c), instead of the exponents. Indeed, with the multiplier the aforementioned, purely mathematical, periodicity of the exponents naturally disappears due to $\mu = e^{(\sigma + \mathbf{i} p\omega_0) T_0} = e^{\sigma T_0}$, for any $p \in \mathbb{Z}$.

2.4. *Time-marching simulations*

In order to compute solutions with unspecified time behavior (*e.g.* not only periodic solutions), we use a classical time-stepping approach to march in time the coupled equations eq. (2.2). A Backward Differences Formula of order two (BDF2) approximates the time derivative:

$$\left.\frac{\partial \mathbf{q}}{\partial t}\right|(t_n) \simeq \frac{3\mathbf{q}(t_n) - 4\mathbf{q}(t_{n-1}) + \mathbf{q}(t_{n-2})}{2\Delta t}$$

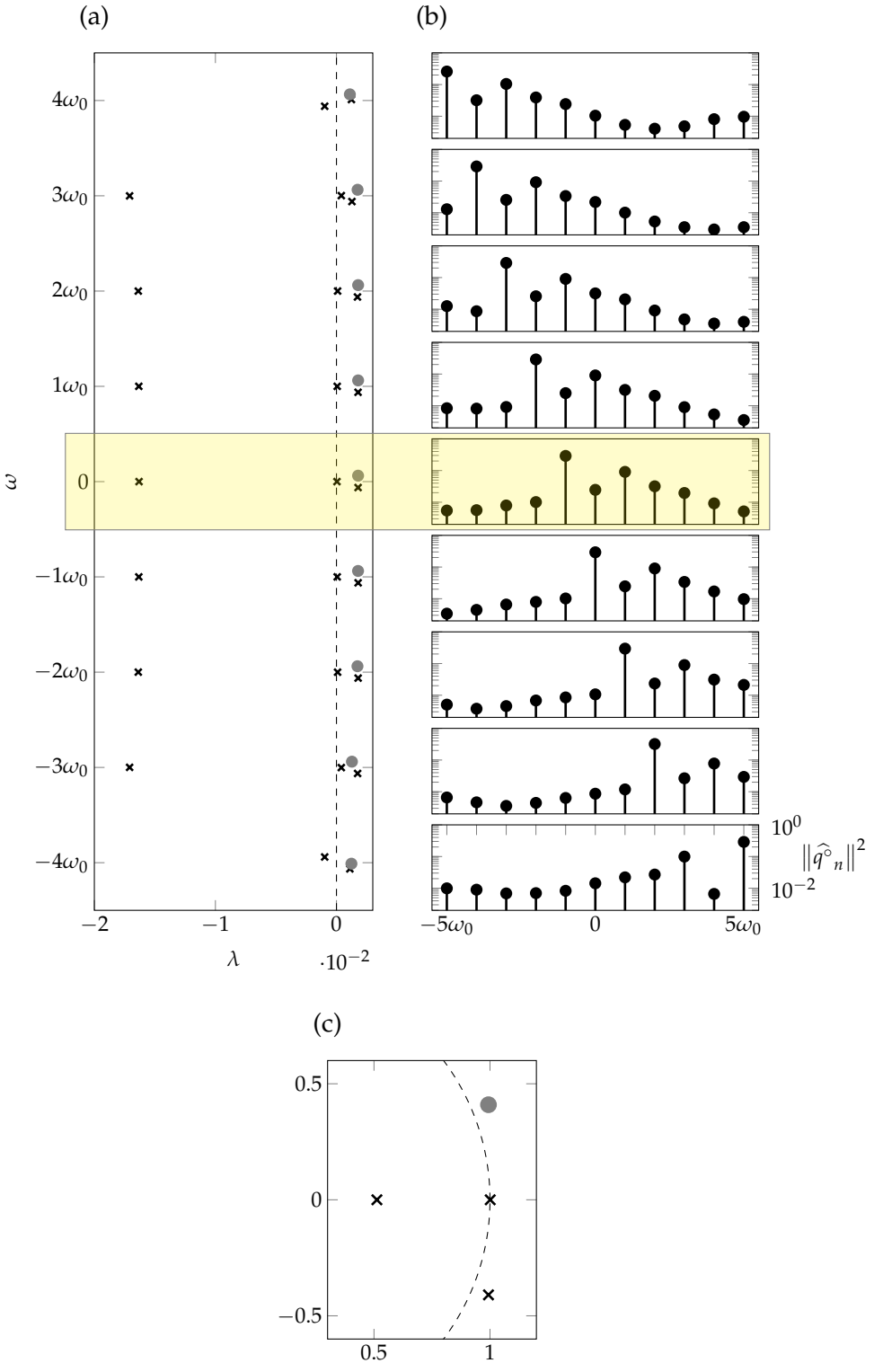

Figure 1: Floquet stability of the base LCO $\mathbf{q}_0(t)$ computed at $U^* = 5.45$. The Floquet exponents obtained as a raw output of a Krylov–Schur run ($s = 1$, $N = 5$) are shown in (a). For a particular exponent marked by a gray disk (and its periodically repeating representations), the Fourier spectrum of the corresponding mode is shown in (b). Due to the periodicity of the exponents, only one pattern (with properly converged modes) is needed to assess Floquet stability (yellow area). In practice, the exponents representation is advantageously replaced by the Floquet multipliers representation (c), where the (mathematical)

yielding the following nonlinear system at each timestep:

$$\frac{3}{2\Delta t}\mathscr{M}(\mathbf{q}(t_n))\,\mathbf{q}(t_n) + \mathscr{R}(\mathbf{q}(t_n)) = \frac{4}{2\Delta t}\mathbf{q}(t_{n-1}) - \frac{1}{2\Delta t}\mathbf{q}(t_{n-2})$$

The latter is solved using the pressure segregation method proposed in Badia & Codina (2007) which consists in mixing a pressure correction approach (Guermond *et al.* 2006) to handle the incompressibility constraint with Dirichlet–Neumann fixed-point iterations for handling the fluid–structure coupling. Solving the implicit nonlinear system is thus decomposed in solving a sequence of simpler linear problems that are: (i) a linear advection-diffusion equation for the fluid velocity, (ii) a Poisson problem for the pressure increment and (iii) a four-by-four linear† solid problem. The fluid problems are space-discretized using the well-known Taylor–Hood $(\mathbb{P}_2, \mathbb{P}_1)$ finite element pair for $(\mathbf{u}, p)$ *via* the finite element library FreeFEM (Hecht 2012). The discrete problems are solved in parallel with preconditioned Krylov subspace methods from the PETSc library (Balay *et al.* 2019), accessed through its FreeFEM interface. More details about the algorithm can be found in **??**.

3. **Results**

From now, we investigate the dynamics of typical section of mass ratio $\tilde{m} = 10^3$, immersed in an incoming uniform flow characterized by the Reynolds number $Re = 500$. As in chapters **??** and **??**, the heaving-to-pitching frequency ratio Ω and the structural damping coefficients, ζ_h, ζ_p are set to $\Omega = 0.8$, $\zeta_h = 0$ and $\zeta_p = 0.05$, respectively. For this set of parameter, we recall that a flutter instability occurs at the critical reduced velocity $U_c^* = 4.96$ (see **??**). In **??**, we showed that the Hopf bifurcation that results from the flutter linear instability is supercritical. The branch of Limit Cycle Oscillation (LCO) emerging at U_c^* is characterized by a low fundamental frequency $\omega_0 \simeq 0.16 - 0.17$. Due to their low frequency, these LCO's are considered as quasi-steady solutions. Now, we investigate the unsteady nonlinear solutions that exist for a reduced velocity significantly above the critical flutter threshold, for U^* between U_c^* and $1.2U_c^*$. Using time-marching simulations, we first explore and characterize in section 3.1 the different solutions that naturally emerge on that velocity range. Depending on the reduced velocity, periodic or quasi-periodic solutions are found. The Time Spectral Method is then used in section 3.2, firstly to compute the LCO solutions that exist on the whole considered range of reduced velocities, and secondly to investigate their linear stability. In section 3.3, we reconstruct the real perturbation associated to the leading pair of Floquet multipliers and analyze it in order to understand the physical mechanism at play in the transition from periodic to quasi-periodic solutions. We conclude in section 3.4 with a detailed comparison of the linear stability (Floquet) results and the fully nonlinear (time-marching) solutions.

3.1. *From periodic to quasi-periodic solutions*

Time-marching simulations are performed on a triangular grid of 15,274 triangles, starting from the steady solution as initial condition. The time step Δt is chosen so that the CFL number $CFL = U_\infty \delta t/\Delta$ (with U_∞ the far-field velocity and Δ the typical size of the smallest triangle) is around 50. This corresponds to about 3000 timesteps per fast period‡ (T_0). The simulations are run for a time long enough so that a permanent regime is reached for each reduced velocity. Figure 2 displays the temporal evolution of the pitching angle and its Fourier spectrum for two values of the reduced velocity. For $U^* = 1.06\,U_c^*$, slightly above the critical reduced velocity, the solution is periodic with a frequency $\omega_0 = 2\pi/T_0 = 0.16$. The amplitude of the harmonic

† The solid dynamics are fully linear due to the elastic axis being at the center of mass
‡ "Fast period" refers in this chapter to the period of the primary flutter instability at U_c^*, see below

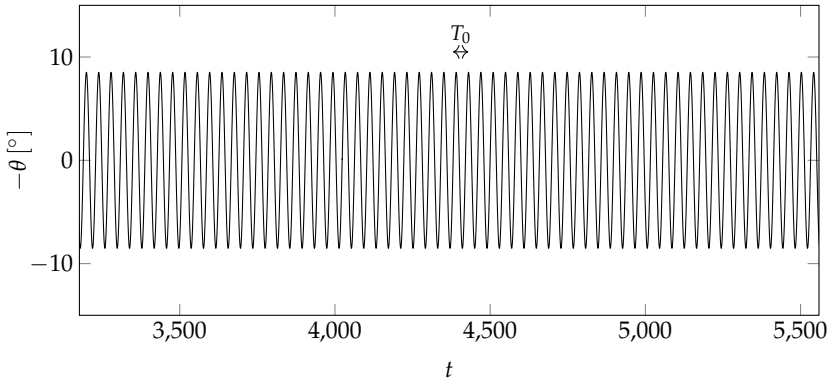

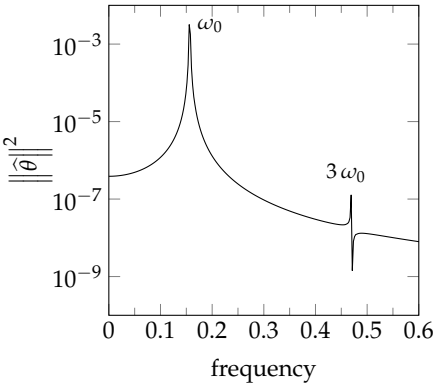

(a) $U^*/U_c^* = 1.06$

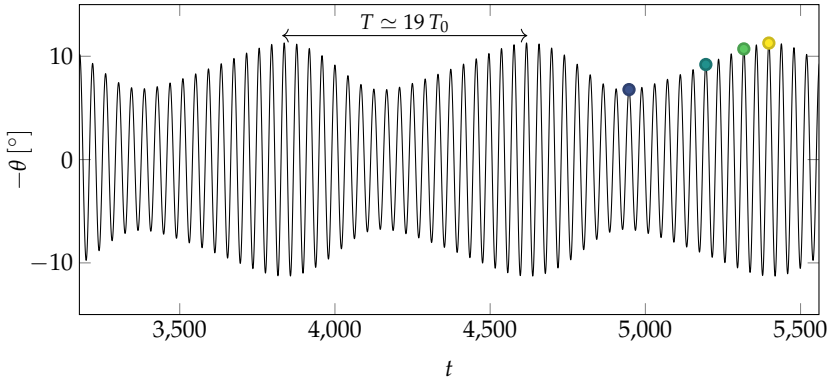

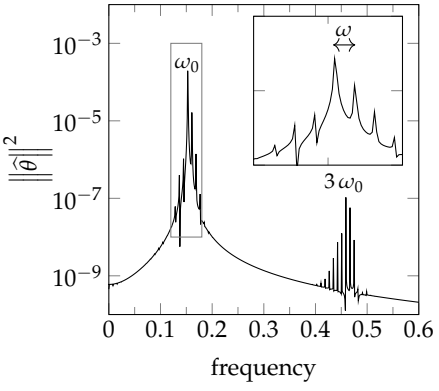

(b) $U^*/U_c^* = 1.10$

Figure 2: (a) Periodic and (b) quasi-periodic oscillations of the pitching angle displayed with time series (left column) and Fourier spectra (right column) for two reduced velocities above the critical flutter velocity U_c^*. ω_0 corresponds to the fundamental frequency of the periodic solution, while ω is the small frequency shift.

oscillating at $3\omega_0$ is very small when examining the pitching angle. However, the periodic LCO is not harmonic since higher amplitude harmonics, not shown here, are observed in the flow. Snapshots of the periodic evolution of the vorticity are shown in fig. 3(a-d). The dynamics consist in a coupled heaving and pitching motion of the plate, typical of the flutter instability. During the plate's oscillation, the flow is mainly attached to the plate, and it is slightly detached only for the highest angle of attack (around 9° here) reached during the plate's oscillation.

When increasing the reduced velocity to $U^* = 1.1U_c^*$, the fast flutter oscillations are still observed in fig. 2(b), but their amplitude is now modulated by a slow frequency $\omega = 2\pi/T$. The spectrum exhibits multiple peaks appearing around the fundamental frequency, at frequencies $\omega_0 - 2\omega$, $\omega_0 - \omega$, $\omega_0 + \omega$, $\omega_0 + 2\omega$, etc ... Since the two frequencies ω and ω_0 are not commensurable ($\omega \simeq \omega_0/19$), this solution is quasi-periodic. The flow evolution of this quasi-periodic solution is shown in fig. 3(e-h) at four instants of the slow period $T \simeq 19T_0$, corresponding to local maxima of the pitching angle. The flow separation is much more pronounced especially in the motion's phase where the plate reaches the largest pitching angle, close to 12° (see fig. 3-h). To gain some more insights in the periodic and quasi-periodic nature of these two solutions,

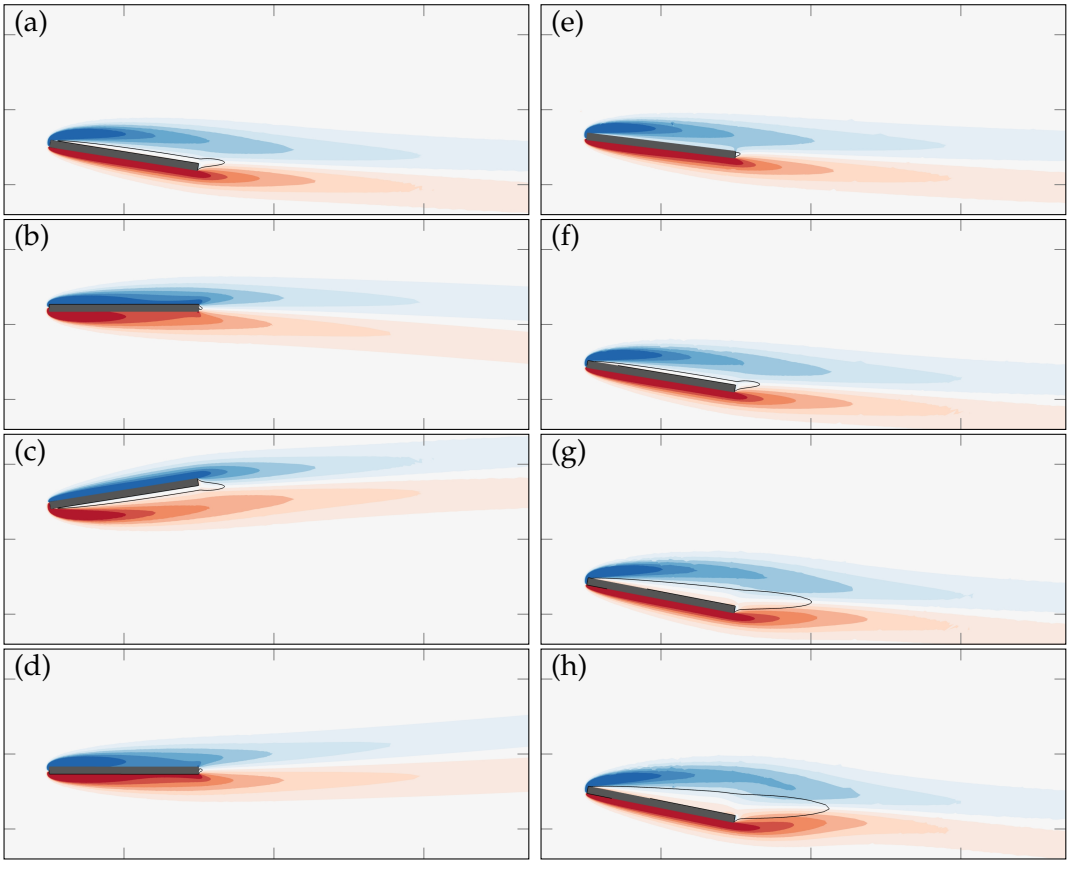

Figure 3: (a-d) Periodic and (e-h) quasi-periodic solutions displayed with the streamwise velocity field. The periodic solution obtained for $U^* = 1.073U_c^*$ is displayed at four instants of the period (a) $t = 0$, (b)$t = T_0/4$, (c)$t = T_0/2$ and (d) $t = 3T_0/4$. The slow evolution of the quasi-periodic solution obtained for $U^* = 1.1U_c^*$ is displayed at four instants (a) $t = 0$, (b) $t = 5T_0$, (c) $t = 10T_0$ and (d) $t = 15T_0$. The thin black curves, corresponding to the contour of zero streamwise velocity, delimit regions of flow recirculation.

we display in fig. 4(a-b) their temporal evolution in the map $\theta - C_L$. The periodic solution (a) evolves on a simple orbit whereas the quasi-periodic solution (b) evolves on a *thick* orbit. Only one modulation period is depicted here, for visualization purpose, but with more slow periods, the orbit visits the whole thickness. To show that this quasi-periodic solution is a torus attractor, the Poincaré sections is displayed in fig. 4(c-d). It is defined as the hyperplane $\{-\dot{\theta} = 0, \ , -\ddot{\theta} < 0\}$, which contains all local maxima of the instantaneous angle of attack. In practice, the Poincaré sections is build by sampling the lift coefficient and pitching angle each time the latter passes through a local maximum. So, by construction, the Poincaré section is a discrete set of points. A total of about 800 fast periods (T_0) — *i.e.* of equivalently 42 slow periods (T) — is computed during the permanent regime in order to build a representative section. The periodic solution, seen in fig. 4(c), is a single point, since the lift coefficient has always the same value when the angle of attack reaches its maximal value. On the other hand, the quasi-periodic solution seen in fig. 4(d) is a closed curve, which is not continuously visited when time grows. This is highlighted by coloring each point of this curve with the time at which it is visited. As time grows, new points are added on that curve without superimposing to a previous one, thus progressively filling

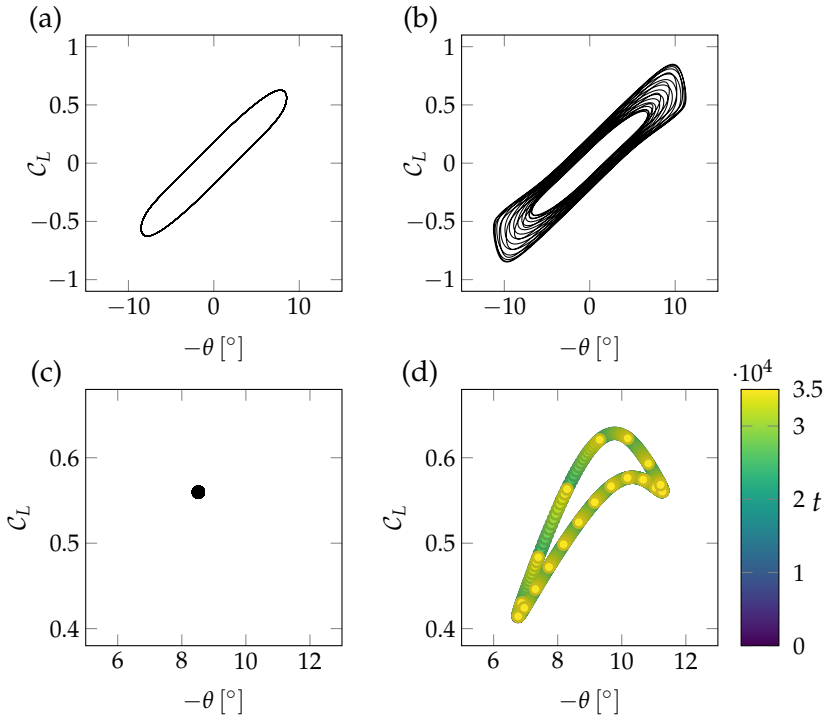

Figure 4: (a-b) Temporal evolution in the map $(-\theta, C_L)$ of the (a) periodic solution at $U^*/U_c^* = 1.060$ and (b) the quasi-periodic evolution at $U^*/U_c^* = 1.10$. (c-d) Poincaré section defined as the hyperplane $\{\dot{\theta} = 0,\ \ddot{\theta} > 0\}$ for the (c) periodic solution and (d) quasi-periodic solutions. Points are colored according to the time at which they where reached.

the closed curve. This shows that the quasi-periodic solution is a torus attractor (*e.g.* (Nayfeh & Balachandran 1995)). Finally, we display in fig. 5 the solutions obtained when varying the reduced velocity in the range $1 < U^*/U_c^* < 1.2$. Maximal values of pitching angles are shown in fig. 5(a) as a function of the reduced velocity ratio. The stable and unstable steady solutions, corresponding to $\theta_{max} = 0°$, are depicted with solid and dashed lines, respectively. We clearly see that a supercritical branch of periodic solutions, corresponding to a single circle for a reduced velocity, emerges above the critical reduced velocity U_c^*, where the steady solution gets unstable. Quasi-periodic solutions, characterized by multiple circles, are obtained when increasing the reduced velocity above $U^* = 1.073U_c^*$. The incommensurate frequencies ω_0 and ω characterizing those quasi-periodic oscillations are shown in fig. 5(b). A slight decrease of the fast frequency ω_0 is observed when increasing the reduced velocity, whereas the modulation frequency ω appears constant, at the scale of the representation (*cf* also fig. 11b)

Those diagrams clearly suggest that, like the periodic LCOs emerge from a linear instability of the steady solution, the quasi-periodic solutions result from a secondary instability, i.e. an instability of the periodic LCO. This scenario is investigated in the next paragraph by performing a Floquet analysis of the periodic LCO.

3.2. *Floquet stability analysis of flutter LCO's*

For reduced velocity $U^* > 1.073U_c^*$, only quasi-periodic solutions are obtained with time-marching simulations. To compute periodic solutions and investigate their linear stability, we use the time spectral methods described in §2.3.

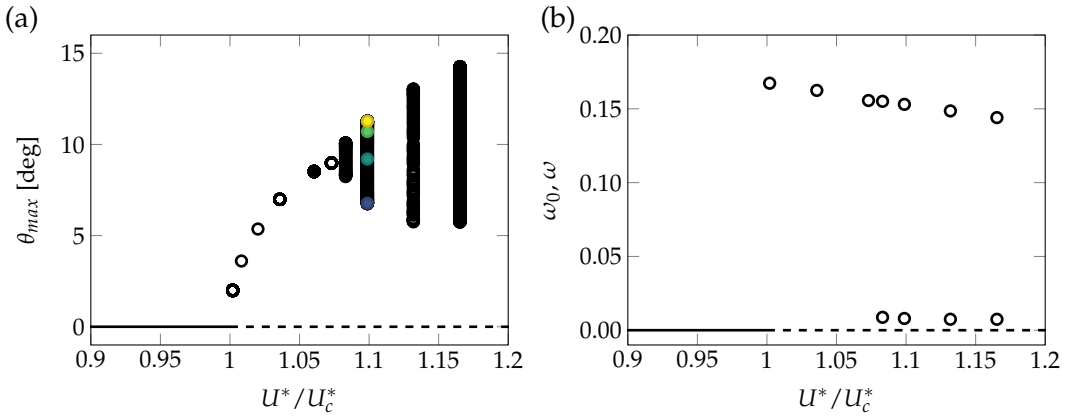

Figure 5: (a) Local maxima of the pitching angle for the periodic (single circle) and quasi-periodic (multiple circles) solutions as a function of the reduced velocity ratio. The filled black circle at $U^*/U_c^* = 1.06$ corresponds to the maximum pitching angle ($-\theta$) of the periodic solution (see fig. 2a) whereas the colored filled circles at $U^*/U_c^* = 1.10$ correspond to four local maxima of the pitching angle in the quasi-periodic solution (see fig. 2b). (b) Fundamental frequencies (circles) of the solutions as a function of the reduced velocity ratio. In the periodic range, only one fundamental frequency ω_0 exists, while in the quasi-periodic range two fundamental frequencies ω_0 and ω are visible. In (a) and (b), the bottom horizontal line corresponds to the steady solution with the plate horizontal (solid when stable, dashed when unstable).

We first examine the accuracy of the time-spectral methods for computing the periodic base solutions and its leading Floquet multiplier by varying the number of harmonics N (equivalently the number of instants $2N + 1$) and the size of the mesh used for spatial discretisation. Up to $N = 20$ harmonics ($2N+1 = 41$ instants) have been used for the computations of periodic solutions as well as Floquet modes. Let us recall that with our TSM solver, the reduced velocity is not imposed in practice as a parameter for computing the base LCO's. Instead, the reduced velocity is an unknown of the computation where an additional constraint is imposed by prescribing the pitching amplitude $\theta_{\max}$. Table 2 displays results of this convergence study for an imposed pitching amplitude, $\theta_{\max} = 10°$. In the upper part of the table, we report first some quantities related to the baseflow: its frequency ω_0, the maximum lift coefficient $C_{L\max}$ reached over a period and the reduced velocity corresponding to the imposed $\theta_{\max}$. For the frequency ω_0, spectral convergence is very fast since only three harmonics are required to capture it up to the fourth significant digits. In comparison, the case $N = 1$ clearly deviates. Convergence of the lift coefficient is significantly more difficult since the convergence of the fourth digit is only reached with $N = 20$. For the reduced velocity, convergence lies in between: easier than for lift but harder than for frequency. Then, we examine the sensitivity of the leading Floquet exponent to the number of harmonics N and grid size. The growth rate converges towards $1.755\,10^{-5}$ (four significative digits) using $N = 10$ harmonics. Except for the erroneous result obtained with $N = 1$, which predicts a stable Floquet mode, the growth rates obtained with a smaller number of harmonics are fairly good. For instance, with only $N = 3$ harmonics, the growth rate is predicted to 2 significative digits. The convergence of the frequency ω is quite similar. Finally, for all quantities considered, doubling the number of triangles in the mesh (from M_0 to M_1) barely modifies the results. Consequently, most of the results shown hereinafter are obtained with the mesh M_0.

The stability of the periodic base solution computed for $U^* = 1.073U_c^*$ is now addressed. This solution is very similar to the one displayed in fig. 2 and fig. 3. The main effect observed on the base LCO when increasing the reduced velocity (not shown here) is the growing pitching and heaving amplitude as well as the widening of the recirculation region. The four leading Floquet

N		1	3	5	10	20
ω_0	M_0	0.14859	0.15316	0.15315	0.15315	0.15315
	M_1	0.14859	0.15315	0.15314	0.15314	0.15314
$C_{L\max}$	M_0	0.6031	0.6886	0.7047	0.7084	0.7083
	M_1	0.6030	0.6886	0.7048	0.7085	0.7083
U^*/U_c^*	M_0	1.12653	1.09980	1.10006	1.10002	1.10002
	M_1	1.12659	1.09984	1.10011	1.10006	1.10006
$\lambda(\cdot 10^{-5})$	M_0	−7.5015	1.7963	1.7866	1.7550	1.7548
	M_1	−7.0844	1.8014	1.7916	1.7559	1.7597
$\omega(\cdot 10^{-3})$	M_0	9.2168	9.5138	9.5379	9.5341	9.5341
	M_1	9.2187	9.5145	9.5388	9.5350	9.5350

Table 2: Effect of the number of harmonics N and mesh refinement M_i on the accuracy of the periodic base solutions (top) and leading Floquet exponent (bottom) both computed with time spectral methods. For all computations, the pitching amplitude is imposed to $\theta_{\max} = 10^\circ$ (U^* is an unknown), as demanded in practice by our TSM solver (*cf* section 2.3). The corresponding reduced velocity of the converged solution is $U^*/U_c^* = 1.10$. For the periodic base solution, we report the frequency ω_0, the maximum lift coefficient, and the reduced velocity. The growth rate λ and frequency ω are shown for the Floquet exponents. The two meshes M_0 and M_1 are made of 15,274 and 28,394 triangles, respectively.

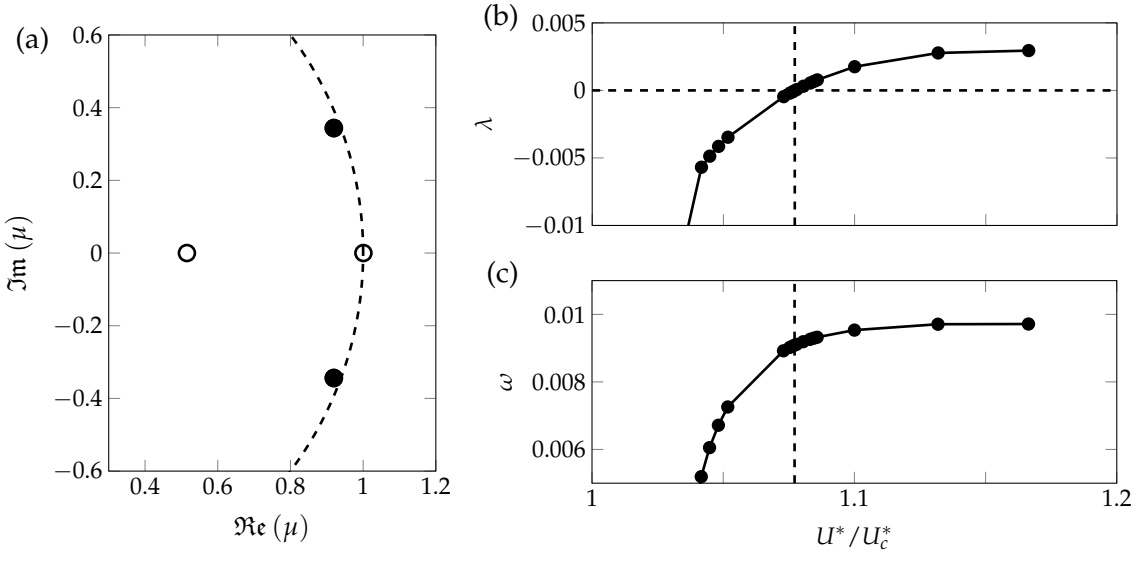

Figure 6: (a) Floquet multipliers computed for the periodic base flow shown in fig. 3 for the reduced velocity $U^*/U_c^* = 1.073$. The stability boundary (unit circle) is depicted by the dashed curve. (b-c) Evolution of the growth rate λ and frequency ω of the leading Floquet mode (black dots in figure a) as a function of the reduced velocity. The mode becomes unstable at a critical velocity $U^*/U_c^* \simeq 1.078$.

multipliers computed for that periodic solution are shown in fig. 6(a). We recall first that the Floquet multiplier $\mu = 1$ is not of interest when addressing the stability of the periodic solution. Indeed, it is easily verified † that the time-derivative of the periodic solution ($\partial \mathbf{q}_0/\partial t$) is an eigenvector of of eq. (2.7), associated to the exponent $\sigma = 0$ (or equivalently Floquet multiplier $\mu = 1$). The Floquet multipliers of interest when addressing the stability of the periodic base flow

† take $\mathbf{q} = \mathbf{q}_0$ in eq. (2.2) and derive with respect to time

are marked with black dots in the figure. In the present case, this is a pair of complex conjugate that gets unstable when increasing the reduced velocity, as seen in fig. 6(b) and (c), showing the growth rate and frequency as a function of U^*/U_c^*. We recall that the frequency of the Floquet mode is associated to the argument ϕ of the Floquet multiplier according to $\omega = (\phi/2\pi)\omega_0$. As clearly visible in fig. 6(b), the argument of the Floquet multiplier is small, and the frequency associated to the asynchronous Floquet mode is also small. For $U^*/U_c^* = 1.100$, we have $(\phi/2\pi) \simeq 0.0622$, indicating that ω is approximately 6% of the fundamental frequency ω_0. From the non-integer value of the ratio $\omega_0/\omega \simeq 16.07$, we see that the new period $T = 2\pi/\omega$ introduced by the Floquet mode is not a multiple of the fundamental period T_0. The oscillating part of the perturbation, defined by neglecting the exponential growth as

$$\tilde{q}(t) = \mathbf{q}^\circ(t)\, e^{\mathbf{i}\omega t} + \text{c.c.} = 2\,[\Re\mathfrak{e}\,(\mathbf{q}^\circ(t))\cos(\omega t) - \Im\mathfrak{m}\,(\mathbf{q}^\circ(t))\sin(\omega t)] \tag{3.14}$$

is thus a quasi-periodic function with two fundamental frequencies†: the low frequency ω introduced by the Floquet exponent and the high frequency $\omega_0 = 2\pi/T_0$ or the ω_0-periodic mode, $\mathbf{q}^\circ(t)$.

The temporal evolution of the quasi-periodic perturbation $\tilde{\mathbf{q}}$ is directly linked to the periodic evolution of the real and imaginary parts of the Floquet mode, $\mathbf{q}^\circ$. More precisely, because ω is much smaller than ω_0, we have $\tilde{\mathbf{q}}(t) \simeq 2\,\Re\mathfrak{e}\,(\mathbf{q}^\circ(t))$ on an interval length T_0 centered on $\omega t \simeq 0$. Similarly, $\tilde{\mathbf{q}}(t) \simeq 2\,\Im\mathfrak{m}\,(\mathbf{q}^\circ(t))$ on an interval centered on $\omega t \simeq \pi/2$. The real and imaginary parts of $\mathbf{q}^\circ(t)$ that are displayed in fig. 7(a-d) and (e-h), respectively, at four instants of the fast period T_0. The flow perturbations of the real and imaginary parts have similar spatial distribution, except at instants of the base flow period when the plate reaches its extrema positions (see figure a and e). At these instants, the flow perturbation is of much larger magnitude and located closer to the plate for the real part of the Floquet mode. We note that such a large flow perturbation is associated to a weak plate displacement (displayed by the orange arrows). This may be attributed to large solid inertial effects due to the high mass ratio used in this study, $\tilde{m} = 10^3$.

The periodic evolution of the plate's displacements is more visible in fig. 8(a-b). First, for both the real and imaginary parts displayed in (a) and (b) respectively, the heaving (squares) and pitching (circles) perturbation evolve harmonically in time. This is also assessed by the Fourier spectrum presented in fig. 8(c) where the first harmonic largely dominates. For the real part, heaving and pitching evolve almost in phase with pitching lagging slightly behind heaving. Oppositely, for the imaginary part, the signals are clearly out of phase with pitching preceding heaving of about $T_0/4$. Focusing on the heaving signal (squares), its magnitude is higher in the imaginary part than in the real part. The opposite is true for the pitching signal. The periodic evolution of the lift (squares) and moment (circles) coefficients are shown in fig. 8(d-e), with the corresponding Fourier spectrum displayed in fig. 8(f). Differently from the solid degrees of freedom, the aerodynamics loads have a more complex time-behavior, typically involving higher harmonics, as shown in the Fourier spectra. Again, a clear difference is observed between the real and imaginary parts. However, this difference seems to be more involved than a simple phase shift (and rescaling), as for the solid components. For example, this can be seen by comparing the respective magnitude of the two local maxima of the lift coefficient in (d) and (e). To evaluate how the dynamics of the real/imaginary parts of the Floquet mode reflects in terms of energy transfer between the fluid and the plate, we show in fig. 8(e-f) the total power provided by the fluid to the solid (thick line) for each part of the signal:

$$\mathcal{P}_{\Re e} = \Re\mathfrak{e}\,(C_L{}^\circ)\,\Re\mathfrak{e}\,\left(u_h^\circ\right) + \Re\mathfrak{e}\,(C_M{}^\circ)\,\Re\mathfrak{e}\,\left(u_\theta^\circ\right)$$
$$\mathcal{P}_{\Im m} = \Im\mathfrak{m}\,(C_L{}^\circ)\,\Im\mathfrak{m}\,\left(u_h^\circ\right) + \Im\mathfrak{m}\,(C_M{}^\circ)\,\Im\mathfrak{m}\,\left(u_\theta^\circ\right)$$

† The question whether these frequencies are commensurable or not cannot be answered with numerical computations. However, the continuous nature of the Poincaré sections obtained in the fully nonlinear regime with time-marching computations (see fig. 4(d)) tend to indicate that they are not.

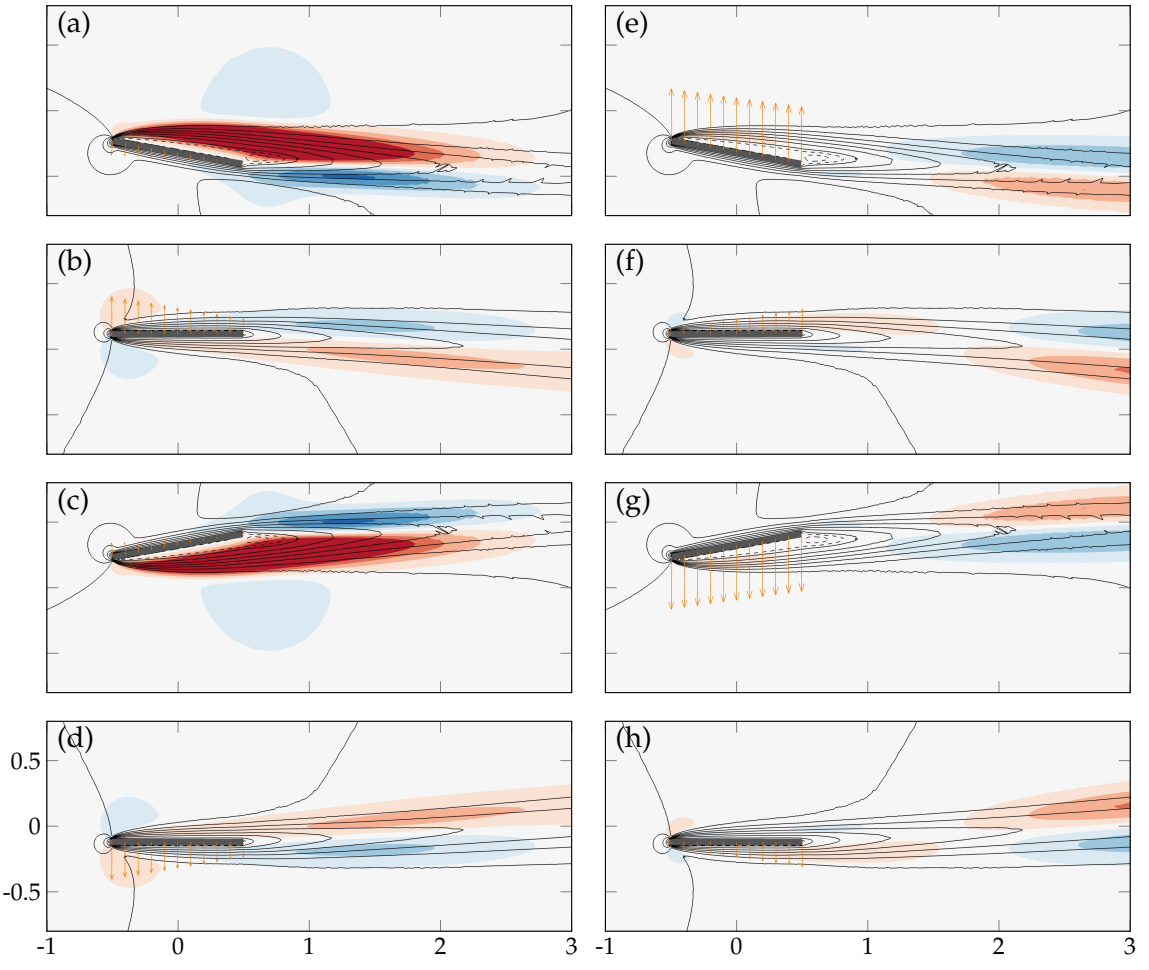

Figure 7: Periodic evolution of the flow and solid displacement fields for the unstable Floquet mode (with positive frequency $\omega > 0$) at $U^*/U_c^* = 1.10$. The streamwise velocity (red and blue) and solid displacement (orange arrows) fields are shown for the (a-d) real and (e-h) imaginary parts of the Floquet mode at instants (a,e) $t = 0$, (b,f) $t = T_0/4$, (c,g) $t = T_0/2$ and , (d,h) $t = 3T_0/4$.

In addition the power associated to the individual heaving (squares) and pitching (circles) motions are represented separately. In both (g) and (h) we first observe that most of the variations in instantaneous power are provided by the heaving power, whereas the pitching power varies only marginally. In addition, the total power is roughly oscillating around zero in the real part whereas it is shifted towards positive values in the imaginary part. As a consequence, the mean power over one period T_0 significantly differs between the two signals. This is shown in (i) where we represent the mean power corresponding to the different signals in (g) and (h) (using the same conventions). For the real part (black), the total mean power is around $0.25 \cdot 10^{-3}$ and is constituted of heaving an pitching contributions of the same order of magnitude. Turning now to the imaginary part (red), the total mean power is about four times higher. In addition, it is entirely provided by the heaving degree of freedom, while the pitching degree of freedom produces zero mean power.

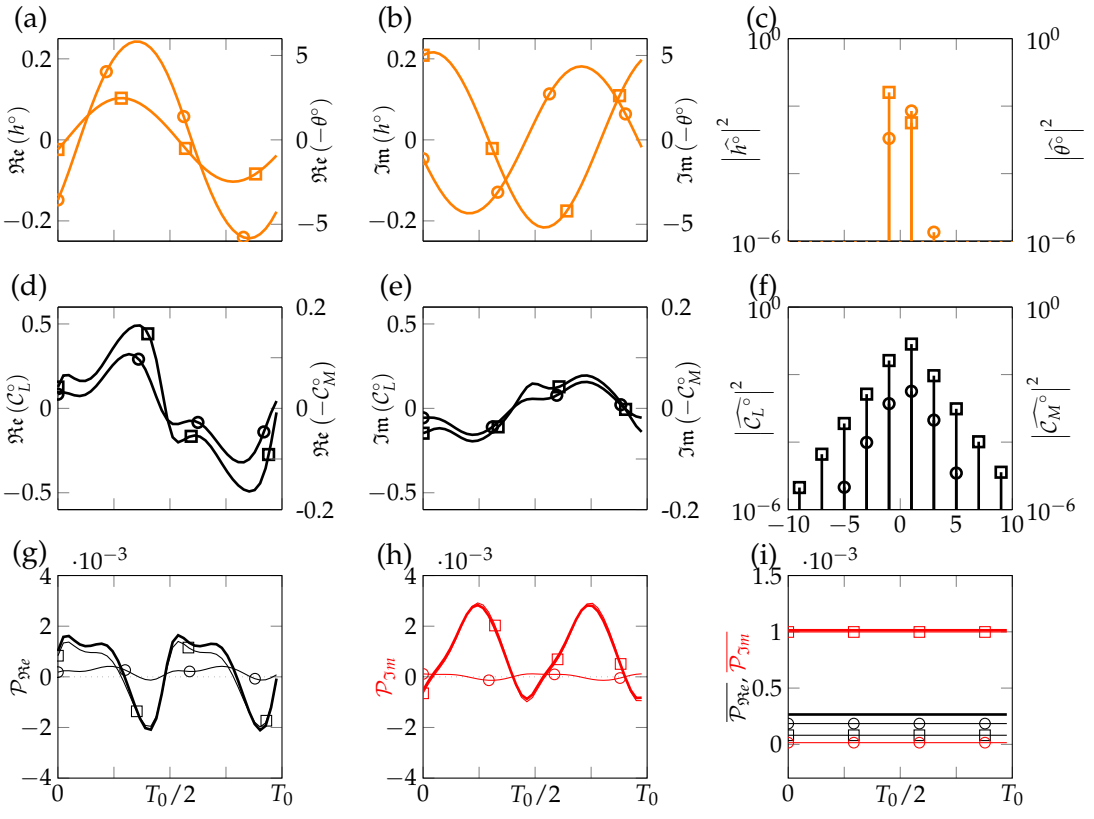

Figure 8: Periodic evolution of the (a-c) heaving (squares) and pitching (circles) components and (d-f) lift (squares) and moment (circles) coefficients for the unstable Floquet mode (with positive frequency $\omega > 0$) at $U^*/U_c^* = 1.10$. (g-h) Instantaneous power provided by the fluid to the solid: total power (thick line), heaving power (squares) and pitching power (circles). The real and imaginary parts of the time signals are displayed in (a,d,g) and (b,e,h), respectively. The modulus of the Fourier harmonics are presented in (c,f). (i) Mean power of the real (black) and imaginary (red) parts of the signal corresponding to the time series in (g) and (f) respectively.

3.3. *Analysis of the quasi-periodic perturbation: a "generalized flutter" instability*

In the previous section, we described the spatio-temporal features of the Floquet mode $\mathbf{q}^\circ(t)$. In this section, we reconstruct the quasi-periodic perturbation $\widetilde{\mathbf{q}}$ (see eq. (3.14)) and investigate its dynamics, allowing us to better understand the physical origin of the low-frequency modulation. These dynamics give rise to what we refer to as a *generalized flutter* instability.

In fig. 9, we present the temporal evolution of the oscillating part of the perturbation, $\widetilde{\mathbf{q}}$, defined by eq. (3.14). The different signals are represented on an interval of $17\,T_0$, which allows to visualize one full oscillation at the modulation frequency ω (we recall the period of the modulation is $T = T_0/(\phi/2\pi) \simeq 16.07\,T_0$). In fig. 9(a), the signal of $\widetilde{h}$ (solid line) and $\widetilde{\theta}$ (dashed line) are shown. They both possess the typical shape of a high-frequency oscillation at a frequency about ω_0, modulated by the low frequency ω. However, the latter modulation is not phased for both signals so that they do not reach their modulation maxima simultaneously. More than that, the phase shift between both signals continuously drifts. This can be seen, for example, by taking the heaving signal as a reference and realizing that the pitching signal is continuously "getting ahead" (*i.e.* shifting to the left) of heaving. Alternatively, we show in fig. 9(b) a measure "per

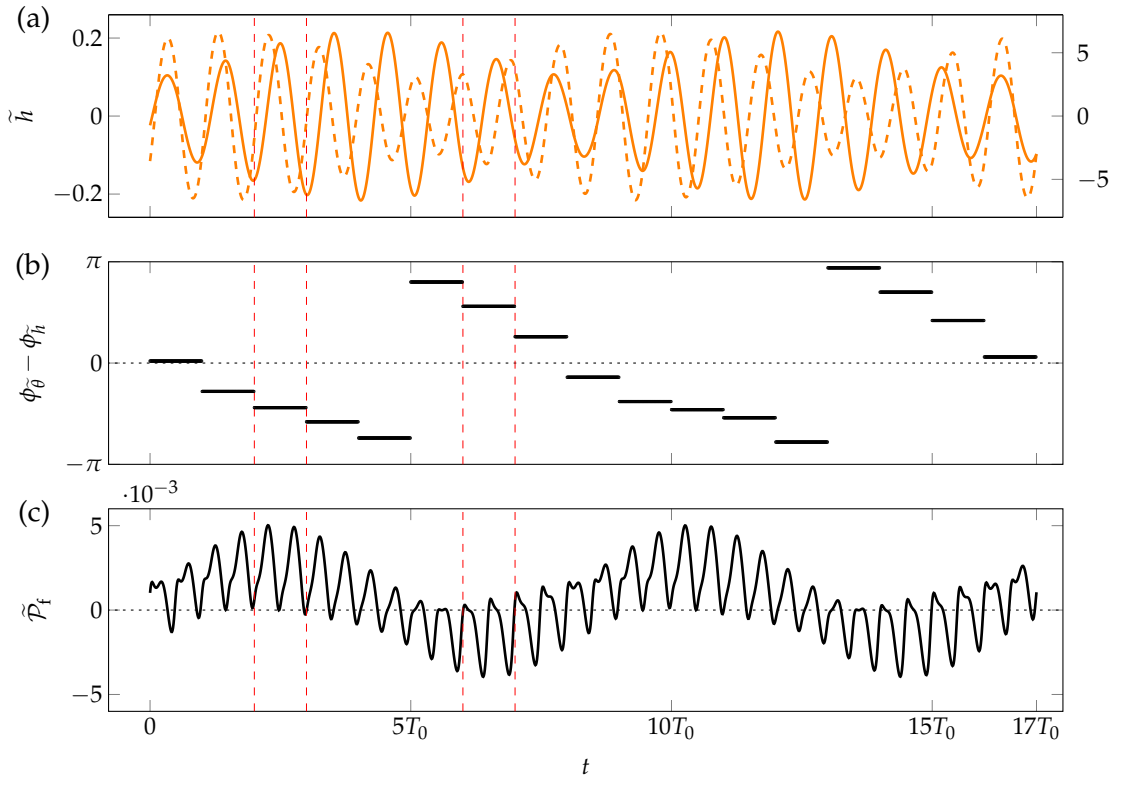

Figure 9: Time representation of the oscillating part, $\widetilde{\mathbf{q}} = \mathbf{q}^\circ(t)e^{\mathbf{i}\omega t} + \text{c.c.}$, of the perturbation generated by the pair of unstable Floquet modes at $U^*/U_c^* = 1.10$. (a) Heaving (solid line) and pitching (dashed line) signals. (b) Average phase shift between pitching and heaving over each fast period T_0. (c) Power transmitted by the fluid to the solid. In all figures, the vertical dashed lines materialize the periods of maximal fluid energy extraction by the solid and maximal solid energy dissipation by the fluid.

fast period" of the phase difference between heaving and pitching. More precisely, the $17T_0$ long signal is divided into 17 subintervals of length T_0. On each of these, the phase difference is measured as the interval of time between the two closest maxima of $-\widetilde{\theta}$ and $\widetilde{h}$. By convention, the phase shift is defined in $[-\pi, \pi]$ and is positive (resp. negative) when heaving (resp. pitching) precedes pitching (resp. heaving). In the figure, it is clearly seen that the phase difference visits the whole interval $[-\pi, \pi]$ (two times, precisely) during the slow frequency oscillation. This continuous drift of the phase shift between heaving and pitching is made possible by the fact that both signals do not dominantly oscillate at the same frequency. This can be seen first by simply counting the number of local maxima in the heaving and pitching signals across the $17\,T_0$ interval of fig. 9(a): they amount respectively to 16 and 18. A second indication of that fact can be deduced from the Fourier spectra of the Floquet mode, presented in fig. 8(c). Indeed, the harmonics of the quasi-periodic perturbation, $\widehat{\widetilde{\mathbf{q}}}$, are directly linked to the ones of the Floquet mode by:

$$\widehat{\widetilde{\mathbf{q}}}(\nu) = \begin{cases} \widehat{\mathbf{q}^\circ}_n & \text{if } \nu = n\omega_0 + \omega \\ \widehat{\mathbf{q}^\circ}^\star_{-n} & \text{if } \nu = n\omega_0 - \omega \\ 0 & \text{else} \end{cases} \tag{3.15}$$

As a consequence, by observing that $|\widehat{h^\circ}_{-1}| > |\widehat{h^\circ}_{+1}|$ in fig. 8(c) (squares), we deduce that

$|\widehat{\widetilde{h}}(\omega_0-\omega)| > |\widehat{\widetilde{h}}(\omega_0+\omega)|$. Conversely, from $|\widehat{\theta^\circ}_{+1}| > |\widehat{\theta^\circ}_{-1}|$ (circles), we obtain that $|\widehat{\widetilde{\theta}}(\omega_0+\omega)| > |\widehat{\widetilde{\theta}}(\omega_0-\omega)|$. Both these analyses reflect the fact that the pitching signal dominantly vibrates at a slightly higher frequency, $\omega_0+\omega$, than the heaving signal which vibrates at $\omega_0-\omega$.

In fig. 9(c), we monitor the energy exchange between fluid and solid through the instantaneous power $\widetilde{\mathcal{P}_\mathrm{f}}$ transmitted by the fluid forces to the solid. It is seen that depending on the phase inside the slow oscillation, the fluid either provides ($\widetilde{\mathcal{P}_\mathrm{f}} > 0$) or dissipates ($\widetilde{\mathcal{P}_\mathrm{f}} < 0$) energy from the solid. For example, between $2T_0$ and $3T_0$, the fluid always provides energy to the solid, whereas between $6T_0$ and $7T_0$, the fluid almost always dissipates solid energy. In average over the modulation period, the fluid provides energy to the solid. By comparing fig. 9(b) and (c), we notice that the extracted power is closely correlated to the phase difference. Indeed, the maximum energy extraction from the fluid ($t \in [2T_0, 3T_0]$) corresponds to a phase difference around $-\pi/2$, whereas the maximum solid energy dissipation ($t \in [6T_0, 7T_0]$) corresponds to a phase difference close to $+\pi/2$.

Let us further explore that link by zooming on the two particular subintervals $[2T_0, 3T_0]$ and $[6T_0, 7T_0]$ in fig. 10(a) and fig. 10(b), respectively. The time signal for $\widetilde{h}$ (solid line) and $-\widetilde{\theta}$ (dashed line) are reproduced from fig. 9, along with snapshots of the instantaneous perturbation pressure field $\widetilde{p}$ (blue isocontours) and perturbation displacement vectors (orange arrows). The black isoline demarcates the recirculation area of the base LCO ($\mathbf{u}_0 \cdot \mathbf{e_x} < 0$). We note that at each snapshot, the fields are represented in the deformed configuration corresponding to the LCO only. In other words, the position of the plate corresponds to $\mathbf{q}_0(t)$ alone. To reconstruct the full displacement of the perturbed solution $\mathbf{q}_0(t) + \epsilon\widetilde{\mathbf{q}}(t)$, one has to add to the represented position of the plate, the perturbation displacement direction materialized by the orange arrows (multiplied by the arbitrary constant ϵ). For the subinterval $[2T_0, 3T_0]$ (a), the perturbation displaces the plate around the LCO position with a movement where the pitching motion precedes the heaving motion by a phase difference around $-\pi/2$ (phase quadrature). From the pressure field, we observe that the flow mostly works positively on the plate. For example at $t = 2\,T_0$ (snapshot (i)), one easily deduces from the pressure distribution on the plate that the moment (calculated around the midchord) is clockwise-oriented. At the same time, the pitching velocity is also clockwise-oriented (*cf* dashed line in the central figure), thus yielding positive work on the pitching degree of freedom. Similarly, at $t = (2+1/8)T_0$ (snapshot (ii)) or $t = (2+2/8)T_0$ (snapshot (iii)), the lift force is clearly oriented upwards, while the heaving velocity is positive; the work on the heaving degree of freedom is then again positive. This intuitively explains why, on average, during the period $[2T_0, 3T_0]$ the solid is extracting energy from the fluid (*cf* fig. 9(c)). Overall, it is remarked the perturbation dynamics described here are highly similar to the one of the classical flutter mode that develops on steady solutions, and that we previously investigated in **??**.

Turning now to the subinterval $[6T_0, 7T_0]$ in (b), the movement presents somehow opposite features. First, the heaving motion now precedes the pitching motion with a phase difference around $+\pi/2$. As a result, from the perturbation displacement vectors (orange arrows), we have the impression of a mode "the other way around" in comparison to (a), *i.e* a classical flutter mode but where the flow would originate from the right. From the pressure fields we observe that the flow now mostly works against the plate's movement. For example, at $t = (6+2/8)T_0$ (snapshot (iii)) or $t = (6+3/8)T_0$ (snapshot (iv)), the lift is clearly downwards, while the perturbation's heaving velocity is oriented upwards (*cf* solid line in the central figure). The opposite situation occurs at $t = (6+7/8)\,T_0$ (snapshot (viii)) with upwards lift and downwards heaving motion. This analysis is in agreement with the average negative power of the fluid forces during the period $[6T_0, 7T_0]$ (*cf* fig. 9(c)). Here, we make the symmetric observation to the one made for (a): the perturbation dynamics on the interval $[6T_0, 7T_0]$ are very close to the (stable) so-called anti-flutter mode that was exhibited in the case of a steady baseflow in **??**.

As a consequence of the above analysis of periods $[2T_0, 3T_0]$ and $[6T_0, 7T_0]$ we can argue that the dynamics of the unstable Floquet mode oscillates on the slow timescale between subintervals

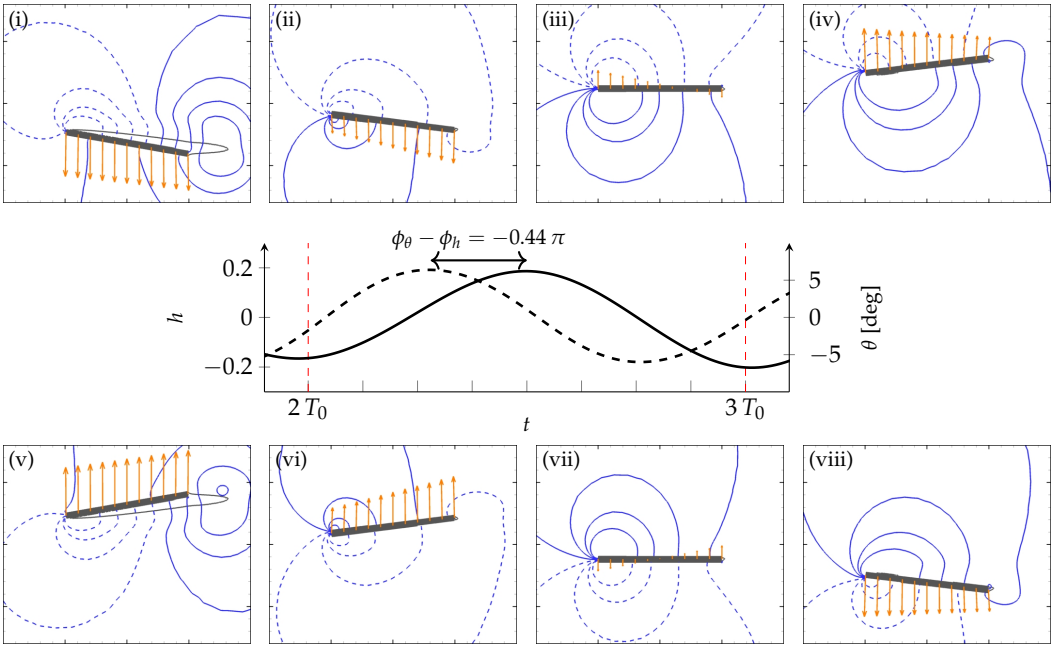

(a) Positive work period

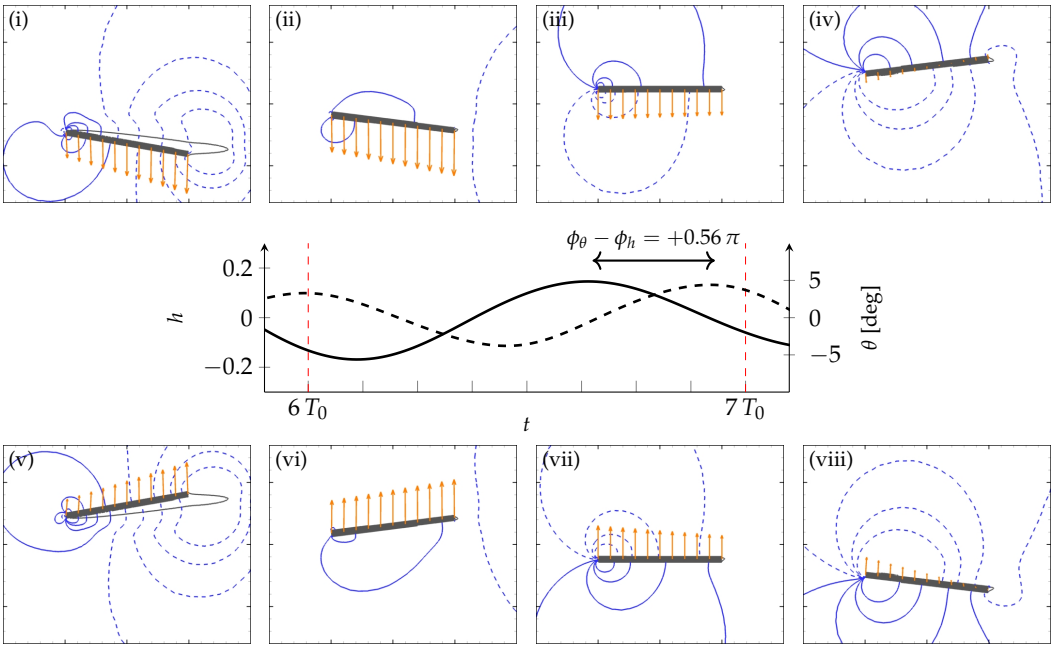

(b) Negative work period

Figure 10: Temporal evolution of the quasi-periodic perturbation on two periods corresponding to (a) maximal fluid energy extraction by the solid and (b) maximal solid energy dissipation by the fluid, both indicated with vertical dashed lines in fig. 9. The heaving and pitching displacement are show with solid and dashed lines, respectively. Snapshots (i) to (viii) are taken at the instants $t = n\,T_0$, $t = (n + 1/8)\,T_0$, ..., $t = (n + 7/8)\,T_0$ ($n = 2$ in (a) and $n = 6$ in (b)). They show the perturbation pressure field (blue contours, negative contours are dashed) and displacement vector (orange arrows). The thin black contour represents the recirculation zone of the LCO. The unperturbed position of the plate is displayed in these figures.

with flutter-like dynamics that provide energy to the solid from the flow, and subintervals with anti-flutter-like dynamics that dissipate solid energy in the flow. During the former, the solid motion amplitude increases, whereas it decreases during the latter, thus yielding a low-frequency amplitude modulation. In other words, the observed instability can be viewed as a kind of generalized coupled-mode flutter that, contrary to the classical one, develops on top of a previously established flutter LCO.

3.4. *Comparison with time-marching results*

After having studied in details the destabilization of the Floquet mode and the associated perturbation, we now wish to compare the Floquet predictions to the reference fully nonlinear time-marching solutions, previously presented in section 3.1.

In fig. 11(a), we start by comparing the pitching amplitude of the periodic orbits computed with TSM (thick lines) to the time-marching results (circles) previously exposed in fig. 5(a). As usual, we represent stable (resp. unstable) orbits with a solid (resp. dashed) line. The bottom horizontal line simply recalls the existence of an unstable steady solution (zero pitching amplitude). For low reduced velocities, where time-marching predicts periodic solutions, TSM and time-marching perfectly agree, as expected. For higher reduced velocities, the time-marching solutions become quasi-periodic in agreement with the destabilization of the TSM solution (dashed lines) occurring at $U^* = 1.078U_c^*$ according to the Floquet stability analysis (*cf* fig. 6). For such high velocities, the agreement between time-marching and TSM is necessary lost on the pitching amplitude as TSM cannot predicts the global maximum reached by the plate across the slow modulation. For example, at $U^* = 1.165\,U_c^*$, the quasi-periodic solution visits the whole range $[5.5°, 14.5°]$, to be compared with the $12°$ predicted by TSM. Still, it can be considered that TSM predicts a "representative" pitching amplitude since the LCO amplitude is always included in the range visited by the quasi-periodic solution. In fig. 11(b), we compare the fundamental frequency ω_0 of the base LCO obtained with TSM (upper solid line) and the low-frequency ω introduced by the unstable Floquet mode (lower solid line) to the two fundamental frequencies of the time-marching solutions (circles). The latter are identified through a FFT analysis of the signal. First, it is observed that the high frequency in the time-marching solutions is in very good agreement with the TSM periodic orbits for all U^*, even when the periodic orbits are unstable (dashed line). This shows that the low-frequency modulation has a very small effect on the fast-frequency ω_0 that is mostly decided by the underlying periodic solution. This is in contrast with the pitching amplitudes shown in (a) that are clearly impacted by the modulation. The low-frequency ω is accurately predicted by the Floquet exponent for U^* close to the instability threshold, $U^* = 1.078U_c^*$, whereas the trend for growing U^* is not accurately captured. Similarly to what happens for the vortex shedding bifurcation around a circular cylinder (*eg.* (Sipp & Lebedev 2007)), this deviation can be safely attributed to the nonlinear effects that come in play when moving away from the instability threshold.

Qualitative reconstruction of the time-marching solutions based on the Floquet mode We conclude this work by showing how superposing the base LCO $\mathbf{q}_0$ and the linear perturbation $\widetilde{\mathbf{q}}$ generated by the unstable pair of Floquet modes compares to the fully nonlinear time-marching solution. First, we must point out an *a priori* inconsistency between the perturbation and the fully nonlinear quasi-periodic time-marching results. Indeed, whereas the perturbation $\widetilde{\mathbf{q}}$ features two modulation amplitude maxima per slow period (see fig. 9(a)), the fully nonlinear solution has only one amplitude maximum per slow period (see fig. 2(b)). To understand and dissipate this apparent discrepancy, we need to reconstruct the perturbed solution $\mathbf{q}_0(t) + \epsilon\widetilde{\mathbf{q}}(t)$, which is the sum of the base LCO and the (oscillating part of) the perturbation. In theory, this quantity is

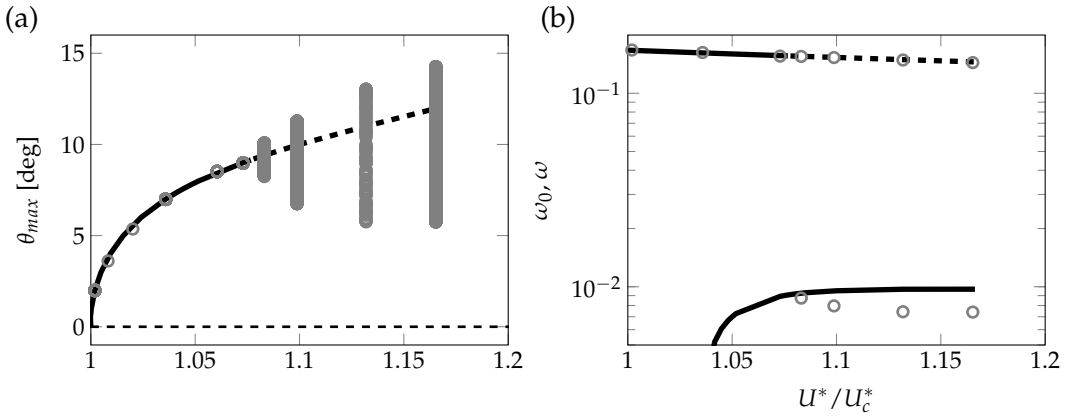

Figure 11: Comparison of Floquet analysis and time-marching results. (a) Bifurcation diagram for the pitching amplitude comparing the periodic orbits computed with TSM (thick lines) to the time-marching results (circles) previously shown in fig. 5(a). (b) Bifurcation diagram comparing the fundamental frequency ω_0 (upper curve) of the periodic orbits and the frequency of their leading Floquet mode ω (lower curve) to the dominant frequencies of the time-marching computations (circles). In both figures, stable (resp. unstable) LCO's are marked by solid (resp. dashed) lines.

— given an adequate amplitude ϵ — a first order approximation of the corresponding nonlinear quasi-periodic solution.

Results of that reconstruction are presented in fig. 12 where we show the pitching components for the LCO $\theta_0(t)$ (thin solid black line), the perturbation $\epsilon\widetilde{\theta}(t)$ (thin dashed black line) and the reconstructed perturbed solution $\theta_0(t) + \epsilon\widetilde{\theta}(t)$ (thick red line) over the same interval of length $17\,T_0$ as in fig. 9. Note that the perturbation amplitude ϵ is arbitrarily chosen for easy visualization. As a consequence, only the LCO solution amplitude has a physical meaning here. By comparing the reconstructed perturbed solution (red line) and the perturbation alone (dashed line) we immediately see that the reconstructed solution yields a signal with only one modulation amplitude maximum per slow period, in agreement with the time-marching results. Looking more closely at the signals, it is intriguing to observe that the maxima of modulation amplitude in the reconstructed solution (in red) do not necessarily match with the maxima of modulation amplitude in the perturbation alone (dashed). For example, around $t = 2\,T_0$, the perturbation is at a maximum of modulation amplitude while the reconstructed solution is close to a minimum. To better understand this feature, it is convenient to think of the reconstructed solution as the superposition of two oscillating signals, θ_0 and $\widetilde{\theta}$, that dominantly oscillate at very close, but different, frequencies: ω_0 for θ_0 and $\omega_0 + \omega$ for $\widetilde{\theta}$ (*cf* the discussion around eq. (3.15)). As a consequence, the phase difference of both signals continuously changes in time, which results in an interference-like phenomenon. When the waves are in-phase — as is the case at the seventh local maximum of the reconstructed solution (see vertical arrow in the figure) — the interference are constructive and the amplitude of the perturbed solution is higher than the amplitude of the LCO alone. On the contrary, when the waves are out-of-phase — as is the case at the fifteenth local maximum of the reconstructed solution (see vertical arrow in the figure) — the interference are destructive and the amplitude of the perturbed solution is lower than the amplitude of the LCO alone. In other words, the amplitude of the reconstructed solution depends only very partially on the amplitude of the perturbation alone; the key dependence is the phase between the base LCO and the perturbation.

In fig. 9(b), we showed that the perturbation $\widetilde{\mathbf{q}}$ is characterized by a continuous drift of the

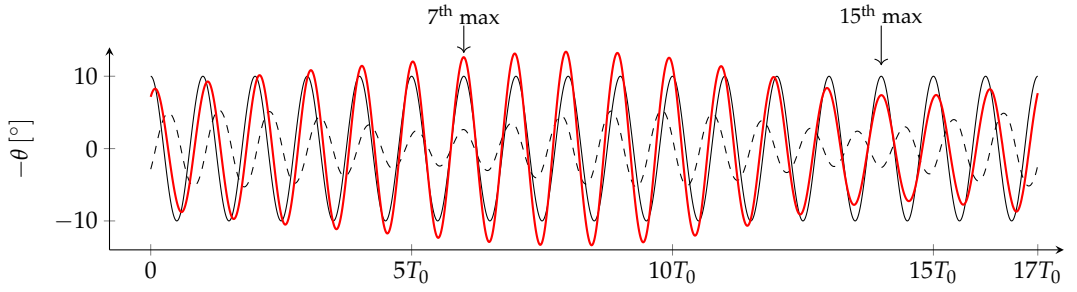

Figure 12: Reconstruction of the full perturbed pitching solution $\theta_0(t) + \epsilon\theta'(t)$ (red line). For comparison, the LCO component $\theta_0(t)$ is shown with thin black solid line, whereas the perturbation component $\epsilon\theta'(t)$ is shown with thin black dashed line. The perturbation amplitude ϵ is arbitrary, for easy visualization.

phase difference between the heaving and pitching motions. This key feature was driven by the fact that pitching vibrates slightly faster than heaving. We now wish to assess if these dynamics are retrieved in the fully nonlinear solutions. In fig. 13, we propose a comparison of the Fourier spectrum of the base LCO $\mathbf{q}_0$ (solid peaks) and Floquet perturbation $\widetilde{\mathbf{q}}$ (dashed peaks) with respect to the fully nonlinear quasi-periodic time-marching solution (gray lines). We focus on a range of frequencies centered on ω_0 since the higher harmonics are negligible in the solid dynamics of the Floquet mode (see fig. 8(c)). Looking first at the spectra of the heaving motion (a), we make several observations. First, the amplitude of the ω_0 harmonic in the quasi-periodic time-marching solution is well predicted by the periodic TSM solution, despite the fact that it is unstable. Second, the dashed peaks $\omega_0 \pm \omega$ coming from the Floquet perturbation are slightly shifted with respect to the time-marching peaks. This is directly linked to the overestimation of the modulation frequency ω with Floquet analysis for reduced velocities as far from the threshold as $U^* = 1.10U_c^*$ (*cf* fig. 11(b)). Third, we notice that several additional peaks at frequencies $\omega_0 \pm n\omega$ are present in the time-marching solution while they are not predicted by the Floquet analysis. This is typically a manifestation of the nonlinear effects that saturate the growth of the Floquet mode away from the threshold. Similar observations can be made for the pitching signal presented in fig. 13(b). Finally, by comparing the $\omega_0 - \omega$ and $\omega_0 + \omega$ peaks in the time-marching heaving signal fig. 13(a), we observe that, aside from the ω_0 component inherited from the flutter LCO, the heaving dominantly vibrates on the $\omega_0 - \omega$ harmonic (the scale is logarithmic, the difference in amplitude between the $\omega_0 \pm \omega$ is about one order of magnitude). It is remarked that this hierarchy between the harmonics amplitudes is retrieved in the Floquet perturbation (squares). A symmetric observation is made in fig. 13(b) for the pitching signal for which both the time-marching solution and the Floquet perturbation agree on the fact that the dominant frequency is $\omega_0 + \omega$. These comparisons show that the difference in the heaving and pitching frequencies, that characterizes the linear Floquet perturbation $\widetilde{\mathbf{q}}$, also characterizes the fully nonlinear quasi-periodic solutions. This arguments tends to show that the linear mechanism described in section 3.3, by which flutter-like and anti-flutter-like dynamics alternate during the low-frequency modulation, is present also in the fully nonlinear regime.

4. Conclusion

This work was aimed at investigating the self-sustained motion of a spring-mounted plate in a laminar viscous flow, above the critical reduced velocity threshold U_c^* at which the classical flutter instability occurs. For the parameters of the study, the flutter bifurcation was supercritical (soft flutter) and gave rise to periodic solutions for $U_c^* < U^* < 1.078\,U_c^*$. Above $1.078\,U_c^*$, the

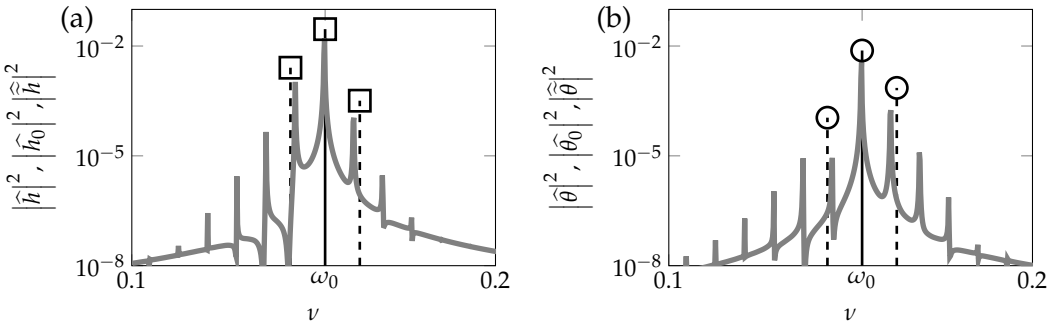

Figure 13: Comparison of the Fourier spectra of the base LCO $\mathbf{q}_0$ (solid peaks) and Floquet perturbation $\widetilde{\mathbf{q}}$ (dashed peaks) with respect to the fully nonlinear quasi-periodic time-marching solution (gray lines) for the heaving (a) and pitching (b) degrees of freedom ($U^*/U_c^* = 1.10$). The amplitude ϵ of $\widetilde{\mathbf{q}}$ is arbitrary.

solutions became quasi-periodic and were characterized by a slow amplitude modulation of the fast flutter oscillations. This transition from periodic to quasi-periodic solutions was investigated by analyzing the linear (asymptotic) Floquet stability of the periodic solutions that underly the observed solution at all reduced velocities. In order to first compute these — possibly unstable — LCO's, and then assess their Floquet stability, we proposed an original approach based on the Time Spectral Method (TSM). For each reduced velocity, the periodic solution was first computed by solving the TSM problem (with unknown frequency). Then, the Floquet stability of the periodic solution was assessed by computing its leading Floquet exponents, that turn out to be the eigenvalues of the linearized TSM operator. Using this method, we showed that the appearance of quasi-periodic solutions is due to the destabilization of a pair of complex conjugate asynchronous Floquet modes. The analysis of the perturbation associated to this unstable pair of modes revealed that the low-frequency modulation was linked to the alternation of fast periods where the mean power of the fluid forces exerted on the solid is positive/negative. During the positive mean power periods, the linear perturbation dynamics were reminiscent of the unstable flutter mode, that develops classically on steady solutions (*cf* **??**), and that is characterized by a pitching-heaving phase shift around $-\pi/2$. On the contrary, during the negative mean power periods, the dynamics of the perturbation resembled the stable, so-called anti-flutter-like mode, for which the pitching-heaving phase shift is around $+\pi/2$. This alternation of flutter-like and anti-flutter-like dynamics was made possible by the fact that the heaving and pitching signals in the linear perturbation do not oscillate at the same frequency. As a consequence, they continuously drift with respect to each other, thus allowing a continuous change of the pitching-heaving phase shift. The last part of this chapter was dedicated to the comparison of the fully nonlinear results from time-marching simulations and the Floquet linear stability results. It was verified that Floquet stability accurately predicts both the reduced velocity threshold for the appearance of the quasi-periodic solutions and, close enough to the threshold, the frequency of the modulation. In addition, we observed in a fully nonlinear solution, far enough from the Floquet instability threshold, that the heaving and pitching signals present different dominant frequencies. This is in agreement with the analysis of the linear Floquet perturbation and tends to show that the mechanism described for the Floquet perturbation is also at play in the nonlinear regime and sustains the amplitude modulation.

REFERENCES

Badia, Santiago & Codina, Ramon 2007 On some fluid–structure iterative algorithms using pressure

segregation methods. Application to aeroelasticity. *International Journal for Numerical Methods in Engineering* **72** (1), 46–71.

Balay, Satish, Abhyankar, Shrirang, Adams, Mark F., Brown, Jed, Brune, Peter, Buschelman, Kris, Dalcin, Lisandro, Dener, Alp, Eijkhout, Victor, Gropp, William D., Karpeyev, Dmitry, Kaushik, Dinesh, Knepley, Matthew G., May, Dave A., McInnes, Lois Curfman, Mills, Richard Tran, Munson, Todd, Rupp, Karl, Sanan, Patrick, Smith, Barry F., Zampini, Stefano, Zhang, Hong & Zhang, Hong 2019 PETSc Web page.

Barkley, Dwight & Henderson, Ronald D. 1996 Three-dimensional Floquet stability analysis of the wake of a circular cylinder. *Journal of Fluid Mechanics* **322**, 215–241.

Deconinck, Bernard & Nathan Kutz, J. 2006 Computing spectra of linear operators using the Floquet-Fourier-Hill method. *Journal of Computational Physics* **219** (1), 296–321.

Deng, Jian & Caulfield, C. P. 2016 Dependence on aspect ratio of symmetry breaking for oscillating foils: Implications for flapping flight. *Journal of Fluid Mechanics* **787**, 16–49.

Dowell, Earl H., Curtiss, Howard C., Scanlan, Robert H. & Sisto, Fernando 1989 *A modern Course in Aeroelasticity*, springer edn.

Elston, John R., Sheridan, John & Blackburn, H. M. 2004 Two-dimensional floquet stability analysis of the flow produced by an oscillating circular cylinder in quiescent fluid. *European Journal of Mechanics, B/Fluids* **23** (1), 99–106.

Floquet, Gaston 1883 Sur les équations différentielles linéaires à coefficients périodiques. In *Annales scientifiques de l'École normale supérieure*, , vol. 12, pp. 47–88.

Gopinath, Arathi K & Jameson, Antony 2005 Time Spectral Method for Periodic Unsteady Computations over Two-and Three-Dimensional Bodies. In *43rd AIAA Aerospace Sciences Meeting and Exhibit*. Reno.

Guermond, J. L., Minev, P. & Shen, Jie 2006 An overview of projection methods for incompressible flows. *Computer Methods in Applied Mechanics and Engineering* **195** (44-47), 6011–6045.

Hecht, F 2012 New development in FreeFem++. *J. Numer. Math.* **20** (3-4), 251–265.

Hill, G. W. 1886 On the part of the motion of the lunar perigee which is a function of the mean motions of the sun and moon. *Acta Mathematica* **8** (1), 1–36.

Jallas, Damien, Marquet, Olivier & Fabre, David 2017 Linear and nonlinear perturbation analysis of the symmetry breaking in time-periodic propulsive wakes. *Physical Review E* **95** (6), 1–15.

Jian, Zhang & Jinwu, Xiang 2009 Nonlinear Aeroelastic Response of High-aspect-ratio Flexible Wings. *Chinese Journal of Aeronautics* **22** (4), 355–363.

Krack, Malte & Gross, Johann 2019 *Harmonic Balance for Nonlinear Vibration Problems*.

Lazarus, Arnaud & Thomas, Olivier 2010 A harmonic-based method for computing the stability of periodic solutions of dynamical systems. *Comptes Rendus Mécanique* **338** (9), 510–517.

Lee, B. H.K., Liu, L. & Chung, K. W. 2005 Airfoil motion in subsonic flow with strong cubic nonlinear restoring forces. *Journal of Sound and Vibration* **281** (3-5), 699–717.

Lee, B H K, Price, S J & Wong, Y S 1999 Nonlinear aeroelastic analysis of airfoils: bifurcation and chaos. *Progress in Aerospace Sciences* **35**, 205–334.

Li, Xiaoguang & Fleeter, Sanford 1997 Dynamic stall generated airfoil oscillations including chaotic responses. *Collection of Technical Papers - AIAA/ASME/ASCE/AHS/ASC Structures, Structural Dynamics and Materials Conference* **1**, 11–23.

Liu, G., Lv, Z. R., Liu, J. K. & Chen, Y. M. 2018 Quasi-periodic aeroelastic response analysis of an airfoil with external store by incremental harmonic balance method. *International Journal of Non-Linear Mechanics* **100** (December 2017), 10–19.

Liu, Liping & Dowell, Earl H 2004 The Secondary Bifurcation of an Aeroelastic Airfoil Motion: Effect of High Harmonics. *Nonlinear Dynamics* **37**, 31–49.

Nayfeh, Ali Hasan & Balachandran, Balakumar. 1995 *Applied nonlinear dynamics : analytical, computational, and experimental methods*. Wiley.

Peletan, Loïc, Baguet, Sébastien, Torkhani, Mohamed & Jacquet-Richardet, Georges 2013 A comparison of stability computational methods for periodic solution of nonlinear problems with application to rotordynamics. *Nonlinear Dynamics* **72** (3), 671–682.

Pfister, Jean-Lou, Marquet, Olivier & Carini, M. 2019 Linear stability analysis of strongly coupled fluid–structure problems with the Arbitrary-Lagrangian–Eulerian method. *Computer Methods in Applied Mechanics and Engineering* **355**, 663–689.

Saad, Youcef 1993 A Flexible Inner-Outer Preconditioned GMRES Algorithm. *SIAM Journal on Scientific Computing* **14** (2), 461–469.

Shaabani-Ardali, Léopold, Sipp, Denis & Lesshafft, Lutz 2019 Vortex pairing in jets as a global Floquet instability: modal and transient dynamics. *Journal of Fluid Mechanics* **862**, 951–989.

Sipp, Denis & Lebedev, Anton 2007 Global stability of base and mean flows: A general approach and its applications to cylinder and open cavity flows. *Journal of Fluid Mechanics* **593**, 333–358.

Zhang, Li & Chen, Fangqi 2017 Stability and bifurcation for limit cycle oscillations of an airfoil with external store. *Nonlinear Dynamics* **88** (1), 165–187.